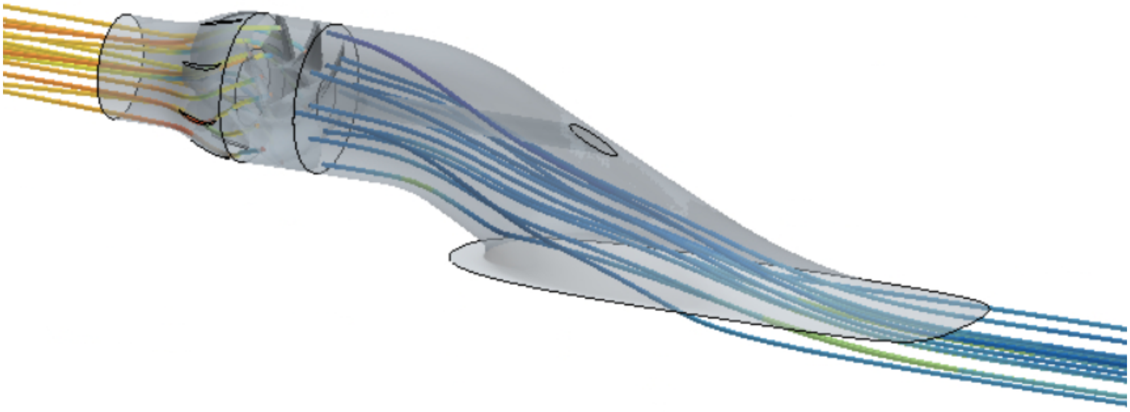

Identification of the Key Parameters for Electric Waterjet Intake Optimization

Joint project with Kongsberg Maritime

Master's thesis in Naval Architecture & Ocean Engineering

Lleo De Ribot Grau
Nuttarat Vichanphruek

DEPARTMENT OF MECHANICS & MARITIME SCIENCES
CHALMERS UNIVERSITY OF TECHNOLOGY
Gothenburg, Sweden 2022
www.chalmers.se

MASTER'S THESIS IN NAVAL ARCHITECTURE & OCEAN ENGINEERING

Identification of the Key Parameters for Electric Waterjet Intake Optimization

Lleo de Ribot Grau
Nuttarat Vichanphruek

Department of Mechanics and Maritime Sciences
Division of Marine Technology
CHALMERS UNIVERSITY OF TECHNOLOGY
Gothenburg, Sweden 2022

Identification of the Key Parameters for Electric Waterjet Intake Optimization
Lleo de Ribot
Nuttarat Vichanphruek

Master's thesis 2022:65 [Ask Study administrator for correct number]
Department of Mechanics & Maritime Sciences
Division of Marine Technology
Chalmers University of Technology
SE-412 96 Göteborg
Sweden
Telephone: +46 (0)31-772 1000

Cover:

Typeset in LaTeX
Printed by Chalmers Reproservice
Gothenburg, Sweden 2022

Identification of the Key Parameters for Electric Waterjet Intake Optimization
Joint project with Kongsberg Maritime
Nuttarat Vichanphruek
Lleo de Ribot
Department of Mechanics & Maritime Sciences
Division of Marine Technology
Chalmers University of Technology

Abstract

Waterjets are commonly used in high-speed crafts because they have better propulsive efficiency compared to conventional marine propellers at high speeds. Nowadays, electric propulsion has been developed worldwide. This brings up the possibility of doing more research on how it can affect the hydrodynamic performance of the waterjet propulsion system. The main objectives of this project are to optimize the waterjet intake, which can maximize the overall system performance, and to investigate the hydrodynamic performance of the entire system when some constraints can be modified due to waterjet electrification. During this research, finding the system performance curve, the effect of extending pump-intake connection study, the effect of shaft removal study, rim-driven impeller study, and intake optimization are carried out. The results show that the intake design and the rotor driving method are directly related to the system efficiency because the inflow to the pump is significantly affected by the intake shape and the shaft. The impeller and the intake should be designed together to match the blades with the specific wake field. To achieve a better inflow to the pump, the key approaches are to lower the intake height and extend the cylindrical part of the intake ahead of the impeller.

Keywords: Waterjet, Optimization, Computational Fluid Dynamics (CFD), STAR CCM+, Capture Area, CAESES, Parameterized geometry, Wake field, Pump Performance.

Acknowledgements

First of all, we would like to thank Arash Eslamdoost for supervising and guiding our thesis project from his excellence and dedicated career in the Hydrodynamic field. For many valuable discussions at his office, and especially for the time he dedicated on teaching us, not only work-wise, also towards our future careers.

We would also like to thank Kongsberg Maritime, specially to the Kristinehamns research center team, Marko Vikström, Reima Aartojärvi, Rickard Gustafsson, Markus Lindholm and Göran Grunditz. Thanks for sharing their knowledge with us and for such a great welcome during our study visit to the Kongsberg maritime research center.

Special greetings to all our classmates for joining us during our journey, enriching and being part of our academic training, as well as for much-appreciated support. Finally, a well-deserved acknowledgment to family and friends.

Nuttarat Vichanphruek and Lleo De Ribot, Gothenburg, July 2022

Acronyms

CFD	Computational fluid dynamics
CAD	Computer-aided design
ITTC	International Towing Tank Conference
MRF	Moving reference frame
NURBS	Non-uniform rational B-spline
RANS	Reynolds-Averaged Navier-Stokes
SST	Shear Stress Transport
WJ	Waterjet

Nomenclature

A	Area, [m^2]
D	Diameter, [m]
g	Gravitational acceleration, [m/s^2]
h	Height, [m]
H	Pump head, [m]
η	Efficiency
L	Length, [m]
$\hat{M}_i$	Momentum flux
n	Normal vector
ν	Fluid viscosity, [Pa · s]
ϕ	Flow rate (non-dimensional)
ψ	head rise (non-dimensional)
θ_t	Start tangential angle
P	Pressure, [Pa]
Q	Mass flow rate, [Kg/s^2]
ρ	Fluid density, [Kg/m^3]
R	Radius [m]
τ	Torque, [Nm]
T	Thrust, [N]
T_w	Wall shear stress
V	Velocity , [m/s]
w	Width, [m]
ω	Angular velocity of impeller, [rpm]
y^+	Wall distance (non-dimensional)
ξ_{v_a}	Pump inflow uniformity
ϕ_p	Perpendicularity
V_a	Axial velocity, [m/s]
V_t	Tangential velocity [m/s]

Contents

List of Figures

List of Tables

1

Introduction

This section describes an overview of the project, including background on the waterjet propulsion system, objectives, a project structure, and limitations.

1.1 Background

The waterjet propulsion system uses a reaction force created by high-speed water jetting to propel vessels. The waterjet propulsion system draws water from the vessel's bottom and uses a propulsion pump to accelerate the flow and generate thrust using momentum change. Waterjets are commonly used in high-speed crafts because they have a better propulsive efficiency compared to conventional marine propellers at high speed. In comparison to propellers, waterjets are quieter and produce less vibration and noise, which improves not only passenger comfort but also undersea noise and vibration. The system comprises the intake duct, the waterjet pump, the nozzle, and the steering device (Bulten, 2006b).

The waterjet intake is used to connect the propulsion pump and the hull bottom. The cavitation, vibration, and noise performance of the waterjet propulsion pump are significantly affected by the hydraulic performance of the intake. The flow separation loss of the inlet, the constriction loss of the flow channel, the blockage loss, and the friction loss are the key components of the hydrodynamic loss of the intake (Weixuan Jiao et al., 2019). Therefore, it is necessary to find the best intake design for a specific pump at the operating condition.

After passing through the intake, the flow gains a transversal velocity component when it enters the impeller zone due to the impeller's rotation. The impeller-induced transversal velocity becomes the major non-axial component. The non-axial velocity components are considered the energy loss in the discharged jet. In theory, the guiding vanes or stator should remove the flow swirl caused by impeller rotation so that the nozzle released flow contains no velocity components other than the axial component. As a result, the torque applied to guide vanes should be equal to the impeller torque but in the opposite direction (Eslamdoost and Vikström, 2019). The steering device is mounted downstream of the nozzle, which can deflect the jet in order to create steering and reversing forces.

1.2 Objectives

Nowadays, combustion engines often power modern waterjet units. The installation of waterjet propulsion units and their intake design are constrained by the size of the engine and the gearbox. The application of electric drives can reduce the dictated constraints of the conventional waterjet units and thus open new opportunities for modifying the placement of the waterjet unit, the intake design, and the waterjet pump's design. The main objectives of this project are to optimize the waterjet intake that can maximize the overall system performance and to investigate the hydrodynamic performance of the entire system when some constraints can be modified due to the introduction of electric waterjet propulsion. From the two main objectives, this project's goals can be specified in further detail as shown below.

- Develop a parametric waterjet intake model, which can be parameterized for both profile curves and cross sections along the longitudinal position.

- Find the best efficiency of the waterjet propulsion system.

- Study the effect of extending pump-intake connection.

- Study the effect of shaft removal.

- Study the effect using a rim-driven impeller.

- Optimize the intake geometry for maximizing the entire system efficiency.

1.3 Project Structure

At the beginning of the project, a literature review is conducted, so general ideas and knowledge from previous research regarding waterjet propulsion are obtained, and the studies that have been carried out in such investigations will not be repeated. Many papers can be useful for furthering the study, such as the methodology of capture area extraction and waterjet profile curve definition. After that, the parameterized intake duct is developed using CAESES software. The geometries of the entire system have been prepared, including the rotor, stator, intake, tank, and extension pipe. After having the whole domain, CFD simulation can be set up on STAR CCM+. Before starting optimization, the verification and validation of the AxWJ-2, which is the pump used in the simulations are conducted. During optimization, it is good to study and understand the system behavior with certain geometry changes and investigate how the electrification of the waterjet gives room for system geometry changes.

Firstly, in the study, the optimum operating condition of the waterjet system has to be determined. The inlet velocity ratio of the system, which is defined by the pump inlet velocity over the ship velocity, is the indicator for the optimum system operating condition. This ratio can be controlled by the mass flow rate specified at the nozzle exit. After that, the studies of the extending pump-intake connection, shaft removal, and rim-driven impeller are carried out. Finally, the intake optimization study is performed.

1.4 Limitations

The time frame is the first limitation, as the project runs from January 2022 until August 2022. The second is the pump model. The AxWJ-2 waterjet pump from John Hopkins University is used for studying. During this project, this pump model is used in all simulations and studies. Third, the focus of this thesis is to study the water propulsion system itself, so hull interaction effects are neglected. The last limitation is that all the results are from the simulations. Due to a lack of time and equipment, no actual testing is performed.

2

Literature review

In this section, a thorough literature study is conducted. The most interesting sources for our propose are summarised in chronological order.

Bulten (2006b) studies the detailed analysis of a waterjet propulsion system from theory until full scale application. The research shows that the major problem that decreases the system efficiency is the large velocity variation due to non-uniformity. It can cause lower impeller efficiency, cavitation, noise, and vibration due to blade loading variation. There are four reasons that cause non-uniformity. First is the boundary layer ingestion. Second is the deceleration of the flow at the inlet. Third is the shaft inside the intake, and finally the bend of the duct. Different CFD solvers are studied to analyse the flow. The solver that has an ability to capture vorticity is beneficial due to large velocity variation. (Bulten, 2006b) comes up with RANS and wall function methods. The paper does not study more in turbulence models because it is not a goal of the research, so k-epsilon is good enough to close the Navier Stoke equation. The validation of the CFD simulation with the experiment with and without the pump is conducted. Finally, the study performs a full-scale analysis for validation.

Jiang-ming and Yong-sheng (2010) conduct the flow loss of the waterjet intake study. The flow loss of the intake is normally estimated by empirical rules, but the value is over-predicted and might lead to the wrong power prediction. Therefore, this paper introduced the new method to estimate the flow loss to be more precise. The flow loss can be determined by the difference between the total energy at the outlet and the captured area. The mass flow rate at the capture area must be equal to the flow rate at the intake outlet. The capture area can be known if the streamtube is obtained. The streamtube varies with the geometry and operating conditions. The study introduces the method for finding the exact shape of the streamtube. Firstly, the simulation must be done, and the flow field is obtained. After that, a user-defined scalar equation is defined based on the transport equation, considering only the convection term. The internal flow from the outlet of the intake is made by the scalar value equal to one, while the external flow that does not pass through the duct is marked by the scalar value equal to zero. Tracing the streamline backward will give the streamtube shape.

Takai (2010) develops a CFD-based optimization system for waterjets with considering the interaction of a hull. An optimization tool can be done manually or automatically by using an algorithm. There are three main steps. Firstly, a nonlinear problem is solved by forming an objective function and a constraint. Secondly, geometry is generated by the design parameters. Finally, a CFD solver is used to return the values. The paper Introduces many algorithms that help finding a multi-objective design. During optimization, sensitivity analysis is performed manually using a small number of design parameters to obtain the trend toward the objective function. After that, several geometries are selected and applied with a morphing scheme in the optimization loop. This research studies the optimization of the intake duct by varying the lip and ramp structure. The objective is to minimise the friction loss. At the end, merging intake is investigated. The idea is to reduce the wetted surface area that leads to minimising friction loss.

Eslamdoost (2014) studies the physics of waterjet and hull interaction, particularly in the negative thrust deduction phenomenon, and develops a more accurate method for predicting the gross thrust. Two methods are used to model the waterjet/hull interaction. The pressure jump method is the first method, while another one is RANS simulations. Regarding the pressure jump method, the waterjet induces a lower pressure due to the suction process, so the sinkage is increased and leads to the higher resistance. Regarding the self-propulsion RANS method and application, it is found that the difference between gross thrust and net thrust comes from a non-atmospheric pressure at the nozzle exit. Because of a transom wave, the nozzle can be operated in ventilated or submerged condition. Non-atmospheric pressure at the nozzle exit causes the thrust deduction factor to be less than zero. Furthermore, It is shown that the capture area derived from the streamtube is quite different from the shape that the ITTC Specialist Committee on Waterjets proposes. However, the average velocities on the capture area section are still similar. Finally, the capture area is not constant and depends on the operating conditions.

Budziszewski and Friedrichs (2018) research the optimization of an aircraft by the boundary layer ingestion method. This method can reduce power consumption and lead to lower fuel consumption and fewer emissions. The study is done by moving all the propulsors to the rear part of the aircraft and embedding the engines to ingest more boundary layers. When more boundary layer is ingested into the duct, propulsive power can be reduced while the thrust remains constant. There is a drawback to this method due to the fact that more non-uniform flow into the fan will reduce the fan's efficiency. However, it demonstrates that using this method, propulsive power can be reduced by one to four percent.

Huang et al. (2019) proposes a parametric waterjet intake CAD model and finds the optimized intake duct without considering hull interaction by varying four parameters. These varying parameters include slope angle, ramp radius, lip radius, and lip height. The fixed parameters are pump diameter, duct height, and duct length. There are three optimization objectives. The first goal is to achieve as uniform flow as possible at the outlet. The second goal is to have as much perpendicular flow at the outlet as possible. The final goal is to achieve maximum hydraulic efficiency. A sensitivity analysis for each parameter is also carried out. The study shows that the slope angle has a significant effect on the hydrodynamic performance, while the lip height does not affect much. The research also studies the operating conditions with an inlet velocity ratio. It is found that the inlet velocity ratio of 0.6 to 0.8 is the suitable operating condition, otherwise the hydraulic efficiency will drop drastically. Finally, after determining the best design, the model is tested with a mixed-flow waterjet. The more uniform inflow mainly affects the pressure distribution on the impeller suction surface and causes different shaft power.

Weixuan Jiao et al. (2019) proposes a parametric waterjet intake CAD model and finds the optimized intake duct without considering hull interaction by varying three parameters, including duct length, slope angle, and lip structure. No parameters are fixed. The optimization goals are uniform flow, perpendicularity, and maximum hydraulic efficiency. Moreover, the study of cavitation is included. In the beginning, grid convergence is studied, then a validation of the CFD solver with the experimental data is performed and it shows a good agreement with each other. The inlet velocity ratio is studied. The optimized inlet velocity ratio is 0.78 to 0.96. If the intake is operated outside this range, cavitation will occur. A low inlet velocity ratio will have less cavitation risk but will have poor uniformity and separation risk. A high inlet velocity ratio will have better uniformity but also a higher risk of cavitation. After that, ship speed is investigated. The study finds that there is a ship speed limitation and It is limited by cavitation.

Eslamdoost and Vikström (2019) develop a body-force model for waterjet pump simulation. The sliding mesh technique can capture the pump flow physics and is the most accurate approach to represent the pump operation in reality. This paper demonstrates the validation between the sliding mesh technique and the experiment. The result shows a small difference between each other, so the sliding mesh technique is used as the benchmark when studying other pump model techniques. Because pump geometries exist in the sliding mesh technique and the impeller blades have to rotate during the simulation, this method has an extremely high computational cost, and it is not worthwhile to use it for other studies such as waterjet hull interaction. Thus, the moving reference frame technique (MRF) and the body force technique are introduced. The body force technique, in which the stator is present in the simulation and only the impeller blades are neglected, shows quite similar results to MRF, but gradually faster in computational time. Moreover, it can predict the jet stream better. It can be said that the overall performance of the body force technique is better than MRF. In addition, the body force method shows an acceptable result compared to the sliding mesh technique. Furthermore, it is much faster because the impeller is gone. This leads to simpler geometries. Therefore, the body force approach is fast and practical, while the result is still acceptable.

3

Theory

3.1 Characteristic Velocities in a Waterjet

This project proposes the study of waterjet intake optimization. In order to carry out such an investigation, the efficiency of the system should be determined. Therefore, the velocity definitions at specific parts of the entire system are required. Four main velocities can be extracted from fig. 3.1, including ship velocity (V_s), ingested averaged velocity at the inlet (V_{in}), averaged velocity at the pump entrance (V_{pump}), and outlet averaged velocity (V_{out}) (Bulten, 2006b). A good understanding of the figures and velocities mentioned above is crucial for a waterjet performance study. Aspects such as head rise, pressure, efficiency, and thrust are directly correlated to the different flow velocities across the unit.

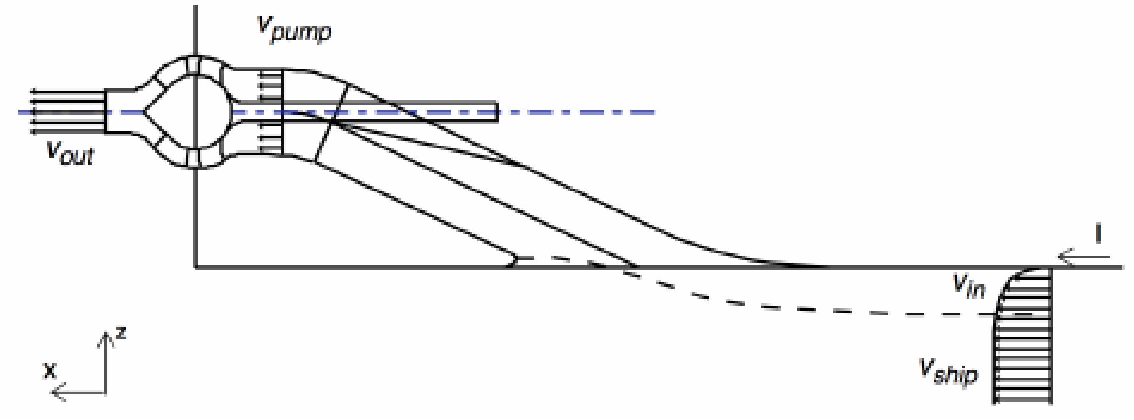

Figure 3.1: Characteristic velocities of a waterjet (Bulten, 2006b)

3.2 Control Volume of the Waterjet Unit

The control volume for the waterjet unit comprises different seven crucial parts numbered in fig. 3.2. From left to right, surface number 1 is commonly named vena-contracta, where the jet reaches its minimum diameter. Right before that, surface number 2 represents the nozzle exit, where the flow exits the waterjet unit. Surface number 3 represents the pump unit. The fourth surface shows the intake duct along with region 5 named "lip" which works as the connection point between the duct and the bottom plate. Surfaces 6 and 7 represent, respectively, the stream tube area and the capture area (Eslamdoost, 2014).

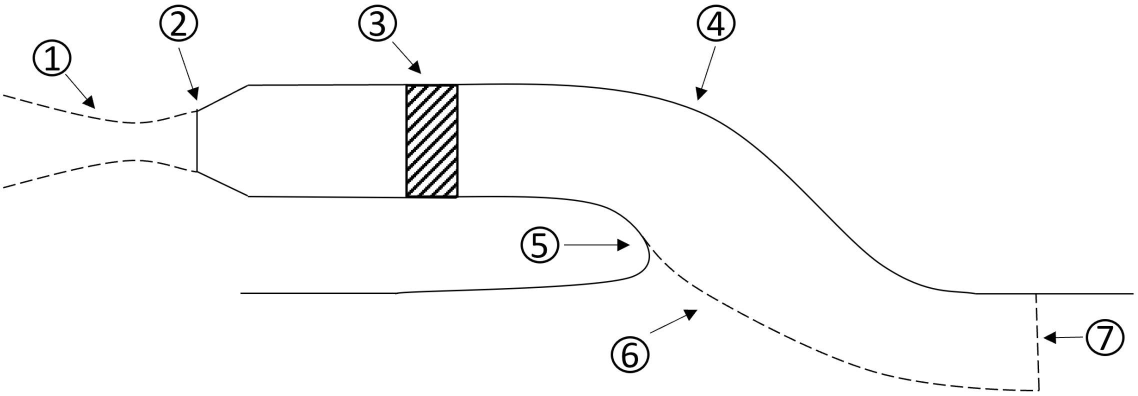

Figure 3.2: Control volume of the waterjet Unit

3.3 Capture Area

The capture area is the region where the flow enters the waterjet system. The capture area provides information on the flow entering the waterjet. The capture area shape varies according to the operational condition. However, the experts (ITTC 2002) developed the methods to estimate the capture area geometry. Regarding this method, it was observed that the width of the capture area is almost constant even if the Froude number is large. Empirical widths of the rectangular and half-elliptical capture areas are shown in fig. 3.3. The height of the capture area varies based on the flow rate through the system, and it is a bit higher in half-elliptical intake geometry compared to the rectangular one (Eslamdoost, 2014).

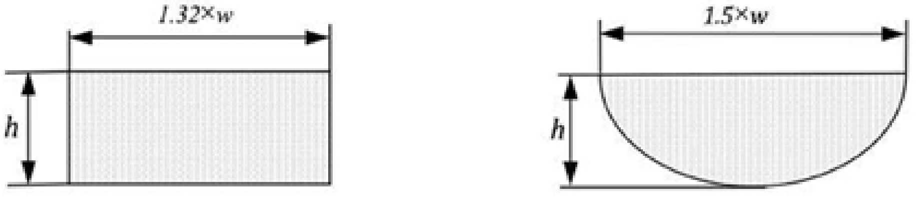

Figure 3.3: Capture area geometry - ITTC Method

Another way to predict the most accurate shape of the capture area is by using CFD. This method requires backward tracing of the streamlines from the pump inlet down to the duct inlet. Fig. 3.4 shows the exact capture area shape from the simulation.

Figure 3.4: Capture area geometry - CFD Method

3.4 Head Rise

The pump head (H) defines the added pressure in a pump due to Bernoulli's principle. Because of the waterjet condition of the pump elevation concerning the inlet, there is an added energy difference, measured in meters as a derivative from the Bernoulli equation (Carlton, 2012).

$$\frac{P_1}{\rho g} + \frac{(V_1)^2}{2g} + H = \frac{P_2}{\rho g} + \frac{(V_2)^2}{2g} + \delta h + h_{loss} \tag{3.1}$$

$$H = \frac{(V_2)^2 - (V_1)^2}{2g} + \frac{(P_2 - P_1)}{\rho g} + \delta h + h_{loss} \tag{3.2}$$

Where in eq. (3.1) and (3.2), P stands for pressure, ρ stands for the fluid density, V stands for fluid velocity at the different measured points, and h defines the height at those sections as shown in fig. 3.5.

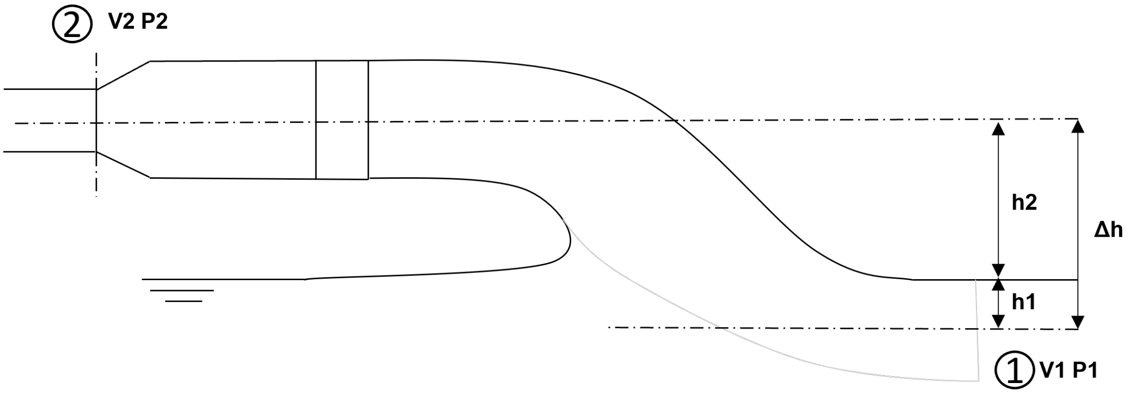

Figure 3.5: Waterjet head rise sketch

3.5 Momentum Flux

From Eslamdoost (2014), the thrust generated by the waterjet unit is always related to the momentum flux variation through the waterjet unit. Why cannot the power of a waterjet be expressed as net thrust? The reason is due to the limitations of measurement methods. The momentum flux change concept can be defined as the change of momentum through the waterjet. The reason is due to the limitations of measurement methods, which measure from the low speed at the intake until the high speed jet at the nozzle exit of the waterjet system. The momentum flux balance on the control volume gives the resultant forces from the waterjet and can be expressed as the following in eq. (3.3).

$$\hat{M_i} = \int \int_A \rho u_i \cdot (u_k n_k) dA \tag{3.3}$$

ρ is the fluid density, u is the velocity, and n is the normal vector to the volume surface.

3.6 Waterjet System Performance

The efficiency of a waterjet unit can be described as the correlation between the pump torque (τ) and the impeller angular velocity (ω), the head of the pump (H) in meters, and the flow rate (Q) in m^3/s.

$$\eta = \frac{\rho g H Q}{\tau \omega} \tag{3.4}$$

It can be also expressed as a dimensionless equation, by adding non-dimensional terms for flow rate (ϕ) as shown in eq. (3.5) and head rise (ψ) as shown in eq. (3.6).

$$\phi = \frac{Q}{nD^3} \tag{3.5}$$

$$\psi = \frac{P_2 - P_1 + \frac{\rho}{2}((V_2)^2 - (V_1)^2)}{\rho n^2 D^2} \tag{3.6}$$

Where P states for pressure and V is the velocity at different measurement points. Extracting the capture area information is an added complex procedure. Therefore, another simplistic and less accurate way to calculate the system efficiency without the need of extracting information from the capture area can be described as the relationship of thrust (T) and torque (τ). However, this method only gives the trend of how efficiency will change. It does not tell the exact number.

$$\eta = \frac{TV_s}{\tau \omega} \tag{3.7}$$

Where V_s is the ship speed and ω for the rotational speed of the pump impeller.

3.7 Impeller Theory

The impeller theory comprises velocity and force components. Figure 3.6 sketches both components schematically. Starting from the velocity components, the triangle is formed by V_a as the flow velocity and the side rotational speed of the impeller, ending with V_r as the resultant velocity of the two previous named components. The triangle of velocities will determine the angle of attack (α), which is an essential parameter for the blade design. On the left-hand side, the force components D represents the drag force, L represents the lift force, and R represents the resultant force combined from the drag and lift force. Finally, torque is the force rotating the impeller and thus generating the thrust (T) needed to power the ship.

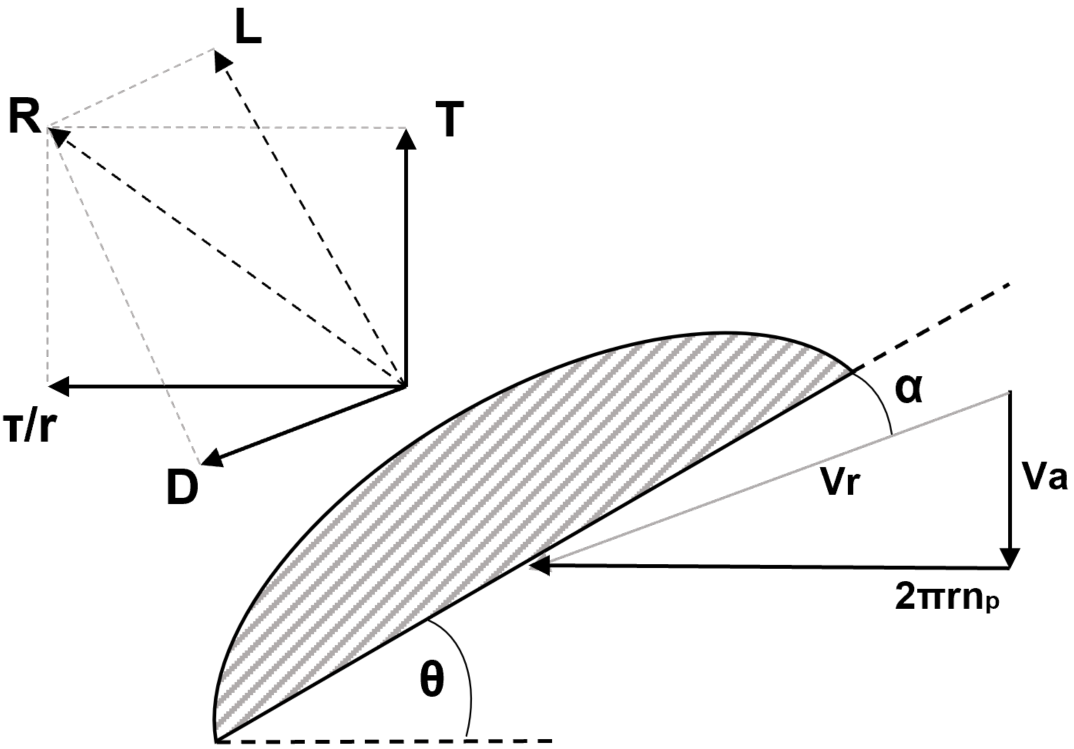

Figure 3.6: Impeller velocity and force components

3.8 Flow Separation

Flow Separation is a phenomenon that occurs due to the three main forces acting on a fluid. This force equilibrium occurs between pressure, inertia, and friction forces. Krause (2005) proposes an example to explain such a phenomenon, assuming a flat plate boundary layer as shown in fig. 3.7. According to fig. 3.7, the flow velocity profile has a point of inflection at the flat plate due to friction forces. The flow static pressure and friction forces slow down the flow near the flat plate. Separation will occur when the velocity of the particle due to the wall shear stress reduces to zero, which can develop a negative direction of the fluid flow.

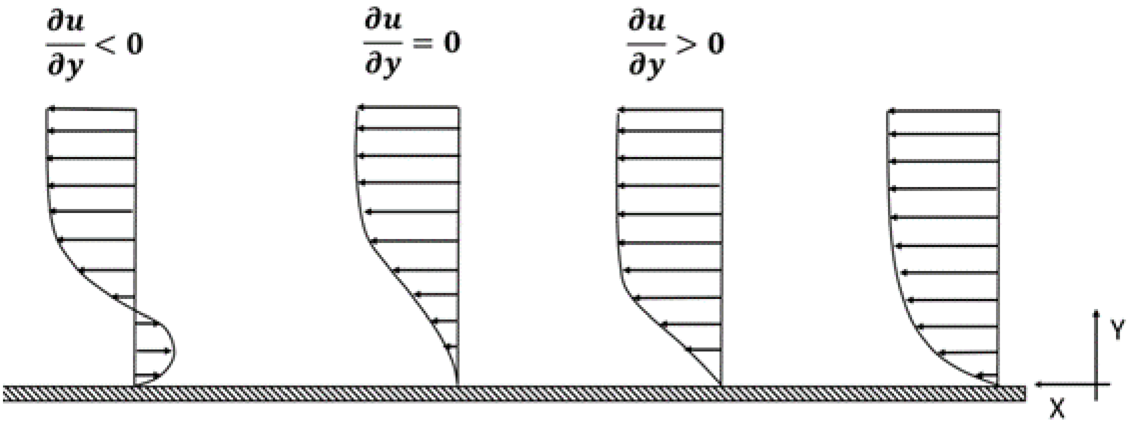

Figure 3.7: Boundary layer flow

Because of the low fluid velocity and the high-pressure gradient at the ramp region, there is a high risk of separation around the ramp region of the duct, as shown in figure 3.8. This risk increases when the inlet velocity ratio is low. The flow separation dramatically affects the inflow to the pump and the pump performance.

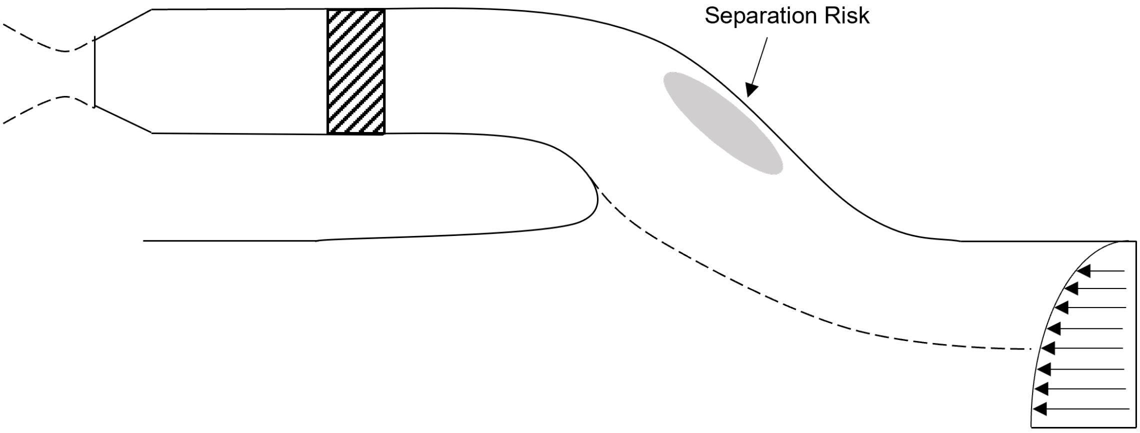

Figure 3.8: Risk of separation

3.9 Tip Clearance

The tip clearance is defined as the gap between the blade of the impeller and the casing. It is the main parameter to take into account for blade design. In shaft-driven impellers, tip clearance is required for correct operation, and it has a direct impact on the system efficiency as it can cause tip leakage and tip vortex, in that way causing potential flow separation to affect the inflow to the impeller (Moon-Chan and Chun Ho-Hwan, 2005). These two effects are the result of the pressure difference between the two sides of the impeller blade. Some flow from the pressure side can be re-directed upstream towards the suction side of the blade. The physic phenomena are further represented in fig. 3.9.

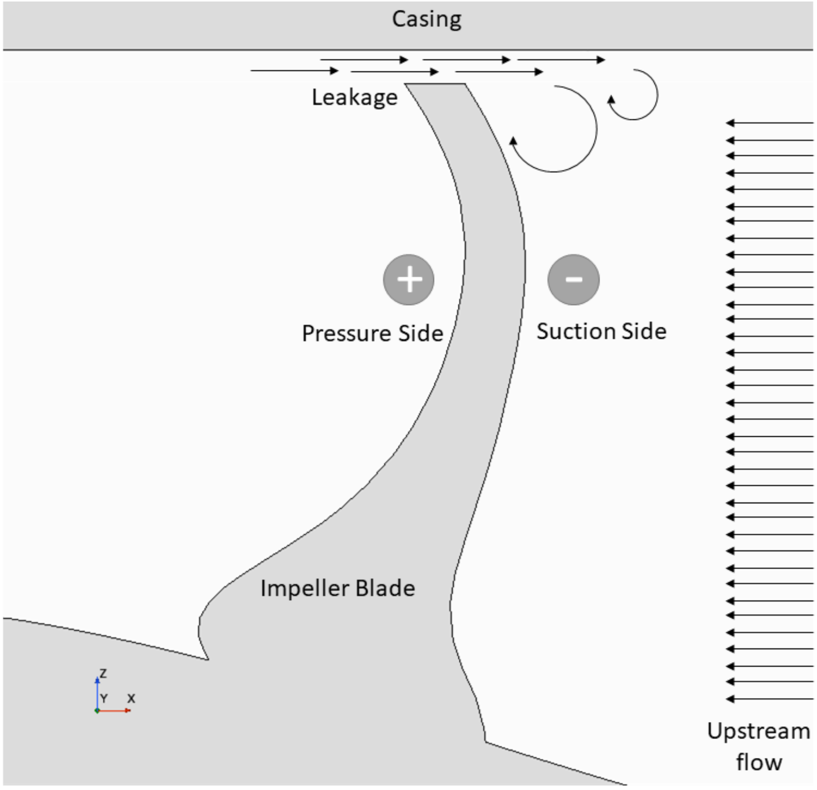

Figure 3.9: Tip Clearance

3.10 Meshing Techniques

Using the right meshing techniques is essential for a successful simulation and obtaining the correct flow characteristics. In this project, three different meshing techniques have been used: prism layer, trimmed mesh, and advanced layer mesher.

3.10.1 Prism Layer Mesher

Prism layer meshing is used mainly to simulate the flow behaviour at the boundary layer, where the flow gets influenced by the wall friction. The boundary layer thickness can be estimated by assuming the logarithmic relationship in eq. (3.8). The following equations are from White (2011).

Log-Law

$$\frac{u}{u^*} = \frac{1}{\kappa} ln \frac{yu^*}{\nu} + B \tag{3.8}$$

where

$$u^* = \sqrt{\frac{\tau_w}{\rho}} \tag{3.9}$$

Reynolds Number

$$Re = \frac{Ux}{\nu} \tag{3.10}$$

where ν is the kinematic viscosity

$$\delta = \frac{0.16x}{Re^{\frac{1}{7}}} \tag{3.11}$$

$$C_f = \frac{0.027}{Re^{\frac{1}{7}}} \tag{3.12}$$

$$y^+ = \frac{yu^*}{\nu} \tag{3.13}$$

3.10.2 Trimmed Mesher

The trimmed mesher cuts and generates hexahedral volume cells from a template mesh. It is commonly applied when the base custom mesh needs to be used or for further improvement of mesh quality for polyhedral grids (Siemens, 2018).

3.10.3 Advancing Layer Mesher

The Advancing Layer Mesher generates a high-quality prismatic cell layer. It is used to generate volume mesh out of prismatic cells next to the wall boundaries, as well as polyhedral mesh elsewhere. The advanced layer mesher improves information from the boundary layer (Siemens, 2018).

4

Methods

4.1 Parametric Geometry Generation

This chapter will introduce how the geometry is generated in CAESES (2019) and the design parameters on which it depends. The main features of the model are to be reliable for geometry parameter changes. A high degree of modification and avoiding abrupt transitions are needed to ensure a good inflow to the pump. All components are dependent on each other to ensure robustness to change.

4.1.1 Profile

As shown in Figure 4.1, the waterjet intake geometry is divided into four different parts, including the horizontal straight pipe, the intake elbow, the ramp, and the lip. Each of these sections is controlled by dependent and independent parameters.

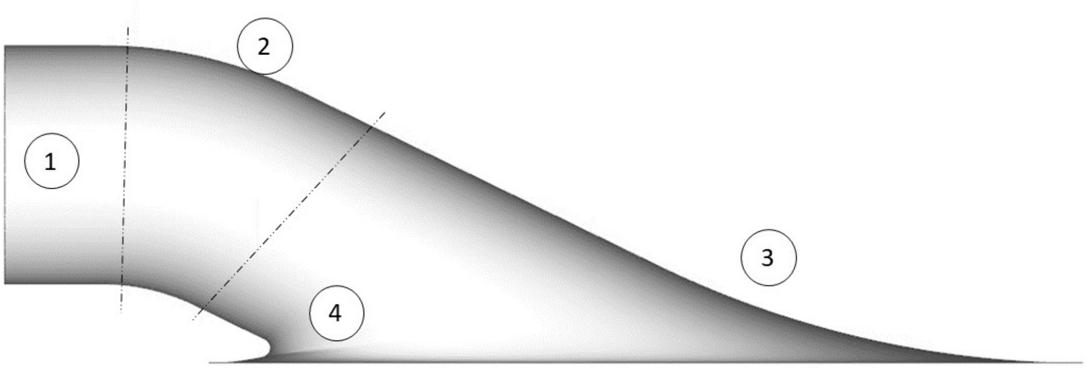

Figure 4.1: Geometry Parts

The horizontal straight pipe length is defined by L_1 and it has an outlet diameter of D. The elbow radius is determined by R_1 and $R_1 - D$. L_2 and R_2 are defined to control the ramp shape. L_3, R_3, R_4, and h_{lip} are used to control the lip shape. Table 4.1 shows the dependency conditions of the different parameters that generate the waterjet intake model.

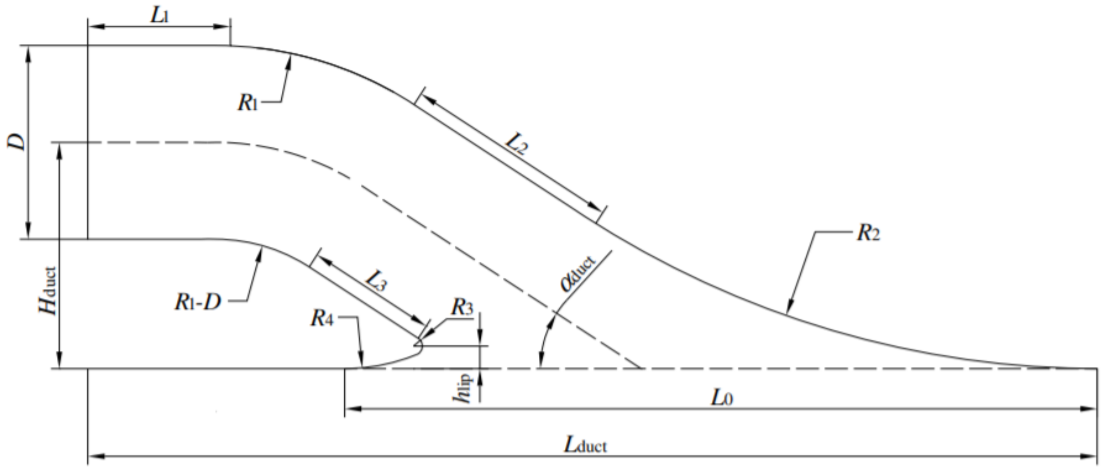

Figure 4.2: Design Parameters of an Intake duct. Huang et al. (2019)

Table 4.1: Profile Design Parameters

Fixed	**Independent**	**Dependent**
L	α (Slope Angle)	L_0
D	R_2	L_1
$R_{3,original}$	f_b (Beam Factor)	L_2
$h_{lip,original}$	H	L_3
H_0		R_1
		R_4
		h_{lip} (Lip Height)
		R_3

The intake duct length (L) and pump diameter (D) are fixed. The independent variables have to be determined for the purpose of generating the model. These independent variables can be used for optimization later on. After defining the values of the fixed parameters and independent parameters, the dependent parameters are calculated by the following equations as shown below. Eq. (4.1), (4.2), (4.3), (4.4), (4.7), and (4.8) are from Huang et al. (2019).

$$L_0 = \sqrt{(R_4 - R_3)^2 - (R_4 - h_{lip})^2} - L_3 \cdot cos(\alpha) - (R_1 - D - R_3) \cdot sin(\alpha) + L - L_1 \tag{4.1}$$

$$L_1 = R_2 \cdot sin(\alpha) - L_2 \cdot cos(\alpha) - R_1 \cdot sin(\alpha) \tag{4.2}$$

$$L_2 = H + \frac{D}{2} - (R_1 \cdot (1 - cos(\alpha) - R_2 \cdot (1 - \frac{cos(\alpha)}{sin(\alpha)}) \tag{4.3}$$

$$L_3 = H - \frac{D}{2} - h_{lip} - (R_3 \cdot cos(\alpha) - (R_1 - D) \cdot (1 - \frac{cos(\alpha)}{sin(\alpha)}) \tag{4.4}$$

$$R_3 = R_{3,Original} - (H_0 - H) \cdot 0.1 \cdot 3 \tag{4.5}$$

$$h_{lip} = h_{lip,Original} - (H_0 - H) \cdot 0.1 \cdot 3 \tag{4.6}$$

$$R_1 = 1.89 \cdot D \tag{4.7}$$

$$R_4 = D \tag{4.8}$$

In order to permit the geometry to handle height modification, which is one of the strong reference parameters for most of the dependent variables, equation (4.5) and (4.6) has been introduced. To avoid cad generation error when optimizing height, this scaling equation modifies parameters h_{lip} and R_3 at the same time, and it uses original values as initial reference parameters.

4.1.2 Cross Section

Another feature required for better geometry optimization is a variable cross-section along with the waterjet intake. Therefore, a cross-section of NURBS curves has been created. NURBS curves are initially defined from three different reference points, A, B, and C, as shown on the left side of figure 4.3. Modifying the position of points A and B will vary the cross-section size, allowing a transition from a circular cross-section to ellipse-shaped sections. The weight factor parameter is introduced to constrain the distance between the curve and the reference point C. In that way, the varying weight factor accomplishes obtaining unsymmetrical and variable corner shapes between the top and the bottom part of the section. An example of the weight factor influence can be found in fig. 4.3. As observed, the higher the weight factor, the closer the curve to point C.

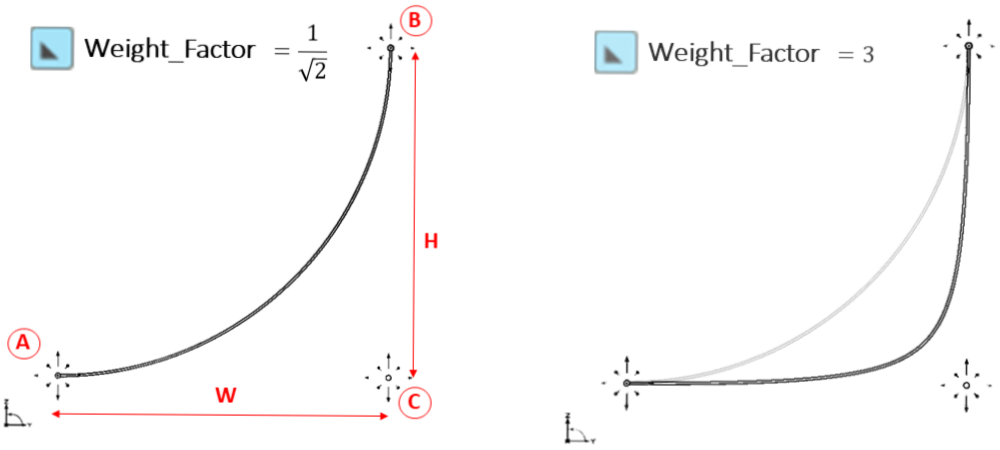

Figure 4.3: NURBS Curves

Table 4.2: Cross-Section Design Parameters

Fixed	**Independent**	**Dependent**
weight bottom area adjust factor	weight top area adjust factor (f_{area})	end tangential angle
weight bottom (w_b)	weight top (w_t)	
Beam factor (f_b)	start tangential angle (θ_t)	
width adjust area		

In order to control the section shape along the duct, engine F-Spline curves are used to determine the value of the design parameters across the length of the intake. The following Figure 4.4 shows two cross-sections, at the outlet and inlet, defined as section A and section B respectively. From Table 4.2 the parameters governing how the reference curves for the cross-section transition from points A to B are presented.

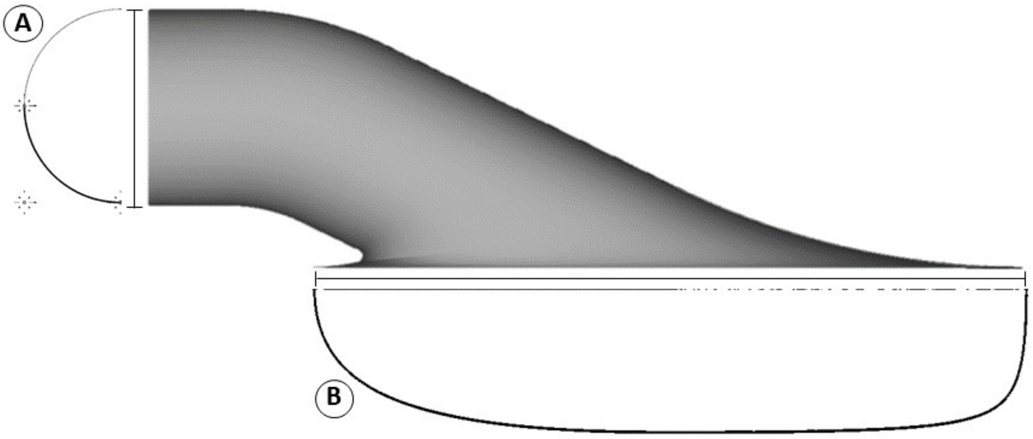

Figure 4.4: Cross-Section Variation

Section A must be a circular cross-section to match with the pump geometry casing, so the values for the weight factor and the width are fixed in the following values:

$$w_t = w_b = \frac{1}{\sqrt{2}} \tag{4.9}$$

$$width = D \tag{4.10}$$

Figure 4.5 represents the reference curves for the cross-section variation. After the initial desired value for the parameter is defined, weight top and bottom take different shape until the inlet position. The ending value of the F-Spline curve will determine the shape of section B as shown before in fig. 4.4. The evolution of the cross-section shape is then defined by the F-Spline curves as shown in fig. 4.5. In that way, a flexible and manageable way of controlling the section is accomplished. As stated in Table 4.2, the top, bottom, and width curves can be further adjusted by modifying the area below the curve. Notice that the weight reference curves for the bottom and top are distinct to obtain asymmetric upper and lower corners if needed.

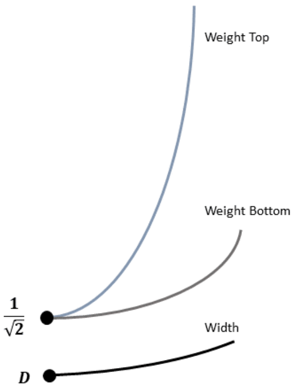

Figure 4.5: Engine Curves for cross-section variation

For a better transition between the inlet and outlet of the intake duct, the weight top area adjust factor can be modified as shown in fig. 4.6. Where the dashed curve 1 represents the original reference curve, and the rest 0.8, 1.2, 2, and 1.5 are possible options for curve area modifications. This adjustment parameter allows a high degree of change in the cross-section transition. Moreover, two more parameters have been introduced to control the starting and ending tangential angles of the reference curves. In that way, more abrupt transitions can also be obtained by setting the start angle to 90 deg, or smoother either way.

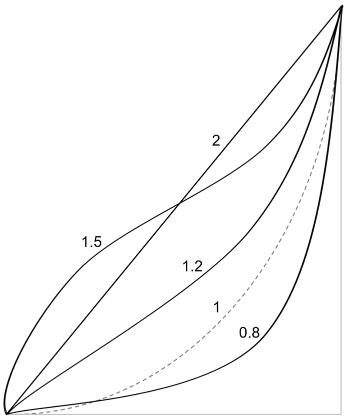

Figure 4.6: Reference curves for cross section transition

4.1.3 Surface

After defining the cross section and profile curves as stated above, a feature definition is created to obtain cross sections at any position along the length of the intake.

Feature definitions are a sequence of commands which help customize curves with specific routines. From these feature definitions, a curve engine is created to further describe the curve cross-sections along the domain and to obtain curves per length of intake.

A meta surface is used to generate the intake surface. The meta surface is the most flexible surface type on CAESES. It lets users design their own parametric surface based on arbitrarily complex curve descriptions. The use of meta surfaces allows a great degree of modification of the surface morphology, which is suitable for optimization studies (CAESES, 2019).

4.2 Pump Geometry and Characteristics

The AxWJ-2 waterjet pump from John Hopkins University is used for studying the intake shape behavior. The AxWJ-2 waterjet pump is an axial flow pump, which has 6 rotor blades. The stator downstream of the rotor has 8 blades. During the simulation, the AxWJ-2 is run at 2000 rpm, which is a design point for an impeller model scale in accordance with Thad J et al. (2008). The main particulars of the pump are depicted in table 4.3.

Casing diameter	305.2 mm
Pump inner diameter	304.8 mm
Outlet diameter	213.4 mm
Rotor	
Number of blades	6
Rotor diameter	303.8 mm
Tip clearance	0.46 mm
Tip profile chord length	274.3 mm
Tip profile axial chord length	127.4 mm
Stator	
Number of blades	8

Table 4.3: The main particulars of the AxWJ-2 waterjet pump

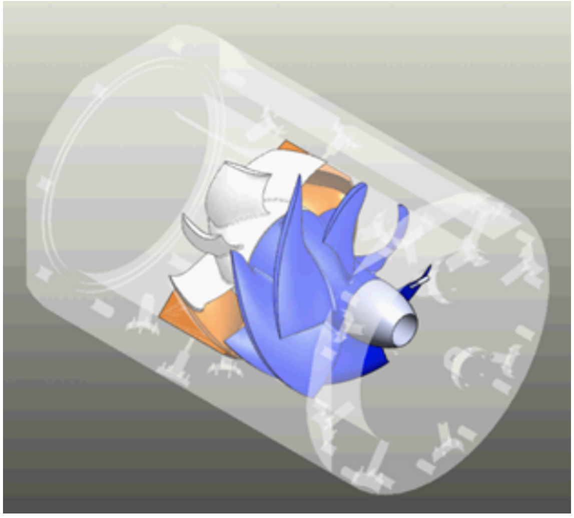

Figure 4.7: AxWJ-2 pump from John Hopkins University

4.3 Set up the CFD simulation

In the following section, computational domain generation, physics model, boundary conditions, pump modeling, mesh generation, and post-processing are described.

4.3.1 Computational Domain Generation

Five regions are generated, including water tank, intake, rotor part, stator part, and extended pipe to appropriately define the boundary condition, mesh, and physics condition. The water tank is the region that mimics the water volume below the hull. It has the reasonable dimension of $30D$ (length) * $10D$ (width) * $8D$ (height), which is recommended by Liu et al. (2010). The intake is located on top of the water tank with the specific location as shown in figure 4.9 recommended by Liu et al. (2010). The pump model from John Hopkins University is modified and divided into two parts. The first part is the rotor region, which has the impeller inside. Generally, this part shall be moving in the sliding mesh approach, but since the moving reference method is used, this part is treated specifically as will mention in section 4.3.4. The second part is the stator region. This region is stationary, and a nozzle outlet is included in the casing. The last part, the extended pipe, which is extruded from the nozzle outlet with a length of $10D$ and has the same diameter as the nozzle outlet. This extended pipe is generated for computational stability as the outlet section boundary shall have a fully developed flow characteristic.

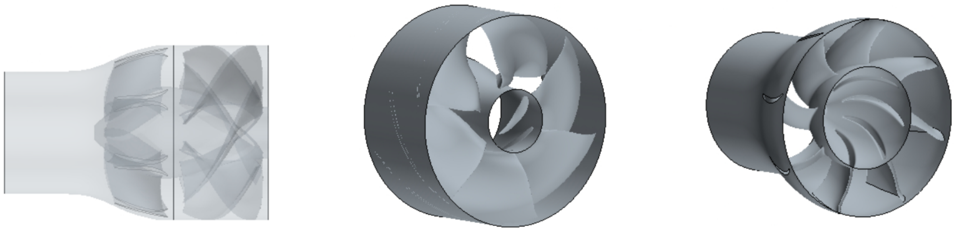

(a) Rotor and Stator (b) Rotor (c) Stator

Figure 4.8: Rotor and Stator regions

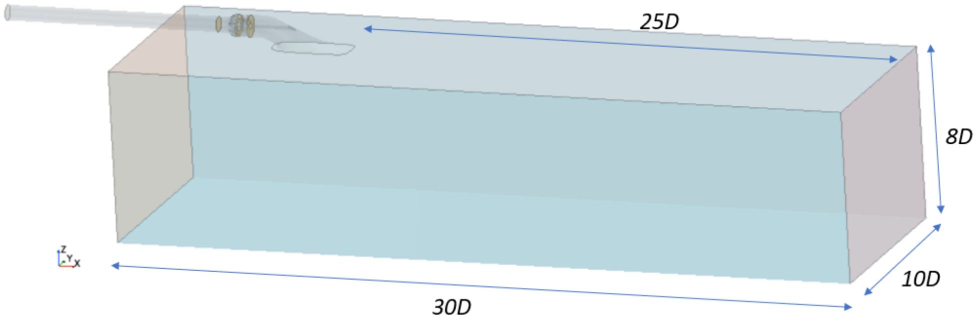

Figure 4.9: Computational Domain

Figure 4.10: Computational Domain (side view)

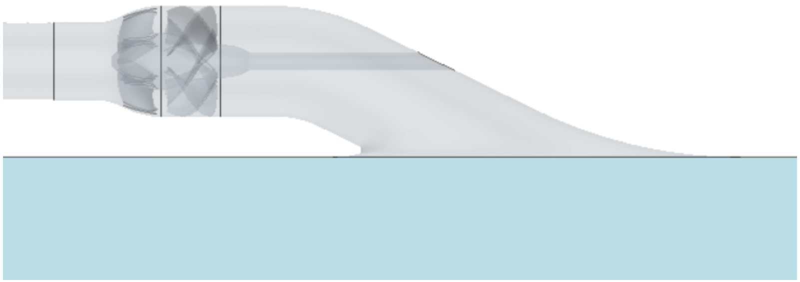

Figure 4.11: Computational Domain (Zoom in)

4.3.2 Physics model

Reynolds-Averaged Navier-Stokes method is used to close the Navier-Stokes equations. The SST k-ω turbulence model is used to simulate the internal flows since it is good enough to predict the flow near a wall and can capture the adverse pressure gradient (Huang et al., 2019). Fluid is water at 15°C. The water density is 999.1 kg/m^3. The water dynamic viscosity is 0.001139 Pa·s. Even though the coupled solver is more robust and faster than the segregated solver, it consumes a lot more memory than the segregated solver. The segregated solver converges quite slow, but requires low memory consumption, which is a good trade off (Siemens, 2018). Thus, the segregated flow solver is selected. Finally, implicit unsteady is chosen, and performed with a time step of 0.01 s.

4.3.3 Boundary conditions

The ship speed of 16.62 m/s will be input as the velocity inlet uniformity into the water tank. To simplify the simulation, the boundary layer of the hull is neglected before the water enters the tank. The outlet of the water tank is set as a pressure outlet equal to the atmospheric pressure, while another outlet through the extended straight pipe is applied as the mass flow rate. The lateral and the bottom wall of the water tank are set as slip walls, so the mesh does not need to be fine there and can reduce the computational time. The top wall of the water tank, which can be considered as the hull bottom flat plate and the intake surface are set as non-slip walls. There are two parts that are needed to input the wall's relative motion. They are the pump housing in the rotor region and the shaft inside the intake. The shaft wall relative motion is equal to the rpm of the impeller, which is 2000 rpm. The pump housing's relative motion is equal to the impeller's rpm as well but in the opposite direction. This part has to cancel the rotation movement from the moving reference frame because the coordinate system is moving around its region, but the pump housing is not moving in practice. The stator region is stationary and regarded as a non-slip wall. The extended pipe wall is considered a slip wall because it is unnecessary to concern the boundary layer around this region. Its responsibility is only to apply the proper outlet boundary condition.

4.3.4 Pump modeling

For the impeller shaft, assigning a wall relative motion can be done easily. However, the impeller region is more complicated. There are three main techniques to simulate the rotation movement of the impeller. There are sliding mesh approach, moving reference frame approach (MRF), and body force approach. All of them have their own advantages and disadvantages that have to be chosen carefully.

Sliding Mesh approach

The sliding mesh technique can capture the pump flow physics and is the most accurate approach to represent the pump operation in reality (Eslamdoost, 2014). Because pump geometries exist in the sliding mesh technique and the impeller region has to rotate during the simulation, this method has an extremely high computational cost. Thus, it is not worthwhile to use it for other studies such as waterjet hull interaction and optimization tasks. Siemens (2018) recommends a time step for the simulation that gives a rotation of 1 degree between each time step. For a rotational speed of 2000 rpm, this will give a time step of $7.88*10^{-6}$s.

Moving Reference Frame approach
The coordinate system for the impeller region is rotated instead of the geometries around the rotational axis with the specific rpm. The impeller is stationary in this method. There is no physical rotation of the geometry within this approach. Thus, this method is less accurate than the sliding mesh approach. It cannot capture the relative position between impeller blades and stator. However, this technique is not dependent on the time step. A larger time step can be used compared to the sliding mesh approach. In this project, a time step of 0.01s is used and it is good enough to have a converged solution. Therefore, the moving reference frame approach is extremely cheaper than the sliding mesh approach.

Body Force approach
For this method, the stator is presented in the simulation and only the impeller blades are neglected, so the computational time is decreased because there is no mesh for the impeller (Eslamdoost, 2014). The virtual disk model then is applied for the impeller region. The axial body force and the tangential body force per unit volume have to be added in the model, so this virtual disk can perform its function as a pump. However, it is tricky to define a proper body force distribution, which will give good flow results that matches with the actual flow.

To sum up, this project is studied about the optimization and there will be various simulations because of the geometry variations. Thus, it is not suitable to use the sliding mesh approach, because this approach is too expensive. Although it is the most accurate method, the time limitation is an important factor to be concerned. In addition, it is difficult and complicated to set up the force distribution for the body force approach to matching with the actual pump flow. Hence, the moving reference frame approach is chosen for this project. It is good enough to predict the flow without taking a too long time.

4.3.5 Mesh generation

There are two mesh types that are used in the computational domain. The first one is polyhedral mesh. It is generated for complex geometries such as rotor and stator. The second type is hexahedral mesh. It is used for simple geometries and is good to satisfy the continuity equation. On top of the base meshing, extra refinements in the computational domain have been created. One upstream refinement, pipe extension refinement, intake refinement, and pump region refinement are presented in fig 4.12.

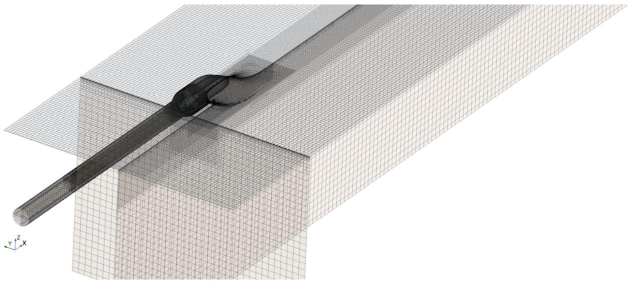

Figure 4.12: Mesh refinement regions

The hexahedral meshing region includes parts of the domain such as intake and shaft, tank, and pipe extension. Prism layer meshing, trimmer mesh, and surface re-meshing are used as meshing criteria. Table 4.4 and Table 4.5 present the main setup features of the mesh used in these parts.

Base Size	20 mm
Number of Prism Layers	16
Thickness of Near Wall Prism Layer	2.4 x 10^{-4} mm

Table 4.4: Coarser Mesh setup parameters

Upstream Refinement	500 %
Pipe extension Refinement	50 %
Intake Refinement	50 %
General Refinement	100 %

Table 4.5: Coarser Volumetric Control Refinement

The polyhedral mesh has been used in more complex geometries such as the pump unit, using the Advanced Layer Mesh method, which is more suitable for complex regions. These pump regions include the impeller, the stator, hub, and casing of such regions. Table 4.6 and Table 4.7 present the main setup features of the mesh used in the pump region.

Base Size	20 mm
Number of Prism Layers	25
Thickness of Near Wall Prism Layer	2.4 x $10^{-}6$ mm

Table 4.6: Finer Mesh setup parameters

Pump and Nozzle Exit refinement	50 %

Table 4.7: Finer Volumetric Control Refinement

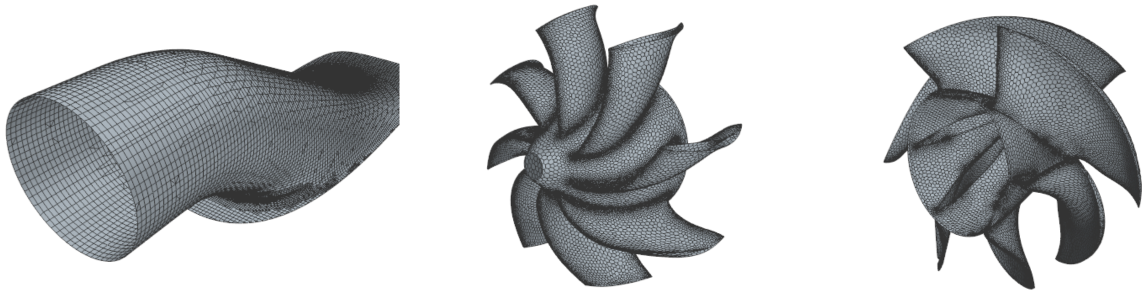

(a) Intake **(b)** Stator **(c)** Rotor

Figure 4.13: Volume meshes of Intake, Stator and Rotor.

Stator	2,404,182
Rotor	1,509,347
Intake + Tank	1,655,922
Pipe Extension	82,714
TOTAL	5,652,165

Table 4.8: Computational domain Number of cells

Figure 4.14 shows in further detail a section plane of three different meshing techniques in the domain. From left to right: pipe extension, pump, and intake.

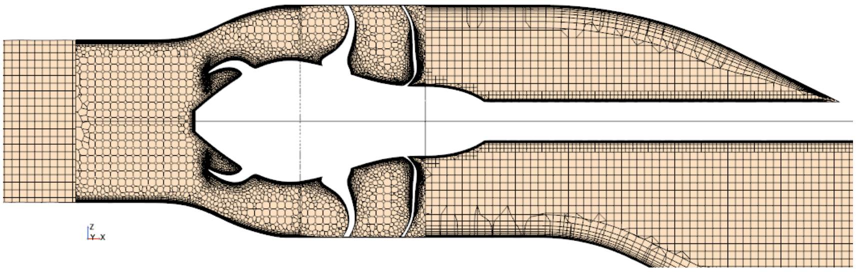

Figure 4.14: Mesh Section representation

4.3.6 Post processing

To visualize the results after the simulation is done, post-processing scenes and reports have to be created.

There are several reports that are needed. The first report is the pressure and velocity report at the inlet and outlet of the pump and at the capture area. Pressure and velocity at the inlet, which can be called the pump upstream section, can be measured in front of the intake end section about $0.1D$, while pressure and velocity at the outlet can be measured at the nozzle exit as shown in the figure 4.15. These values are obtained by finding the average pressure and velocity on those surfaces. The second report is the thrust report, which is generated by the impeller, stator, casing, and intake. Finally, the moment report is created to monitor the impeller torque. With all these data, delivered shaft power, head rise, and pump efficiency can be calculated.

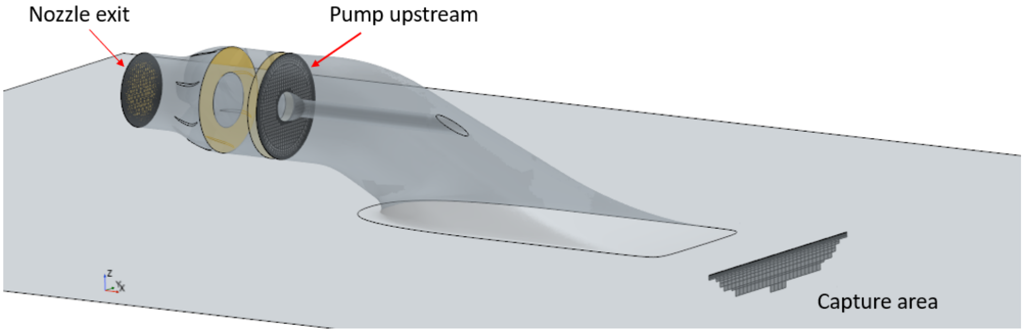

Figure 4.15: Sections representation

The scalar scenes for visualizing pressure and velocity are created. The flow behavior that can be observed in these scenes depends on which sections or parts are selected. For velocity, there are two main components including tangential velocity and axial velocity that can be extracted to understand the flow behavior better. In addition, the wall y^+ scenes are visualized for both pump and domain regions as these values need to be controlled. For the pump region, the wall y^+ value should be less or around 1 for a wall-resolved boundary layer. For the domain region, the wall y^+ value should be above 30, but under 150, so the wall function is applied correctly (Huang et al., 2019). Finally, the vector scene can be plotted as well to visualize the flow direction.

4.4 Capture area extraction

The capture area is unknown until the simulation is done. It can be varied due to intake shape, pump model, and operating conditions. Thus, the special procedure needs to be carried out to extract the capture area for each simulation. The capture area cross section is located one intake diameter ahead of the intake tangency point to the hull as recommended by the ITTC Specialist Committee on Waterjets. To define the capture area shape, an extra passive scalar equation is solved for obtaining the actual geometry of the capture area.

4.5 CAESES coupled with STAR CCM+

The intake geometry is controlled by many parameters. Some parameters, which significantly affect the hydrodynamics performance are picked to study on the intake optimization. In order to run the optimization study, STAR CCM+ has to be coupled with CAESES, so the several simulations due to the geometry variation can be automated. Fortunately, CAESES has the feature named software connection. This connection allows users to connect the CAD modeling with other software including STAR CCM+. Firstly, in the coupling process, the general simulation set up in STAR CCM+ needs to be ready. After that, the users have to record the java macro in STAR CCM+ for telling CAESES what to do and how to run the simulation file in batch mode. During recording the java macro, the intake geometry is replaced, so later on STAR CCM+ in batch mode will understand that they have to run the simulation based on the latest geometry from CAESES. In addition, the simulation results such as figures and physical values can be exported during recording, so the users can visual and analyze the results in CAESES after running various simulations.

5

Verification and Validation

5.1 Set up of AxWJ-2 validation simulation

In order to make sure that the studies have been done correctly related to the quantification of modeling errors, i.e. the difference between the outcome of a mathematical/computational model and the physical reality, the validation is carried out. The aim is to demonstrate that the right equations are chosen. As the AxWJ-2 pump is selected and there is the experimental data available from the John Hopkins University, the CFD simulation results are compared to the experimental data.

The AxWJ-2 pump is tested at the John Hopkins University with a liquid solution of sodium iodide (NaI) in water (62-63 percent of weight). This liquid has a density of 1800 kg/m³ and it has a dynamic viscosity of 0.00198 Pas. Thus, the density and dynamic viscosity of the water in STAR CCM+ is set up to match the experimental fluid properties. The experimental setup is shown below in figure 5.1.

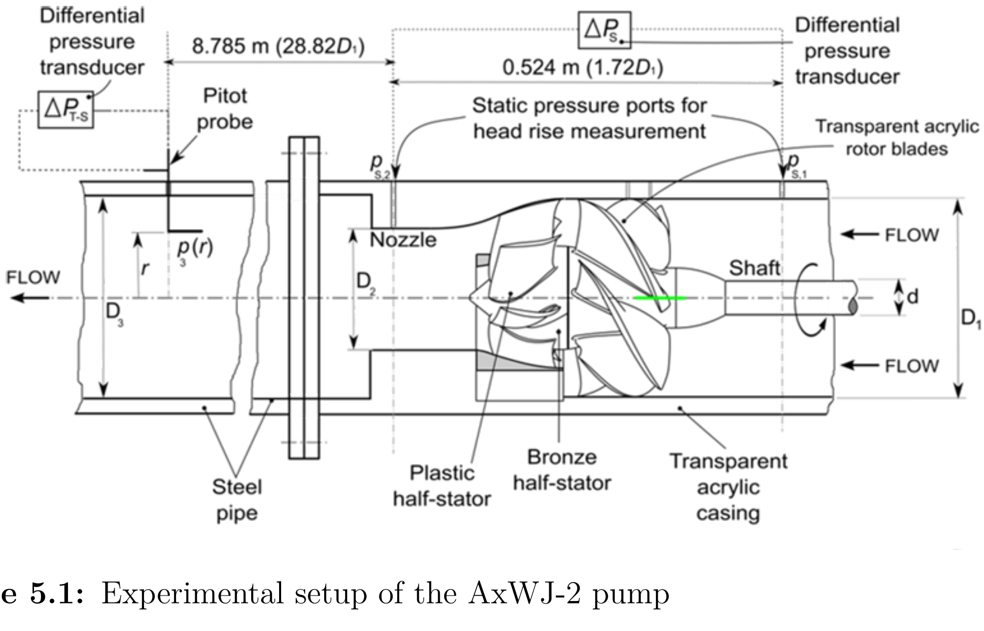

Figure 5.1: Experimental setup of the AxWJ-2 pump

To validate the simulation properly, the experimental setup at the John Hopkins University is imitated in STAR CCM+ as shown in figure 5.2. In order to obtain the head rise from eq. (6.1), The inlet velocity and inlet pressure can be defined from the average values on the cross section before the pump inlet, while the outlet velocity and outlet pressure can be defined from the average values on the cross section surface at the nozzle exit. The positions of the cross section are matched with the experimental measuring positions. Rotational rate of the impeller (ω) is fixed at 900 rpm. The impeller thrust and torque (τ) can be extracted from the simulation.

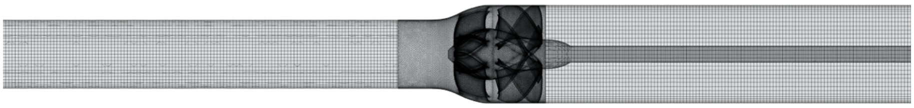

Figure 5.2: Setup of the AxWJ-2 pump in STAR CCM+

The range of the inlet velocity to the domain is calculated backward from the eq. (5.1) as the flow rate coefficient range is known from the experimental measurement. Thus, the results from the simulation will be in the same range as the experimental data. To compare the results with the experiment, the head coefficient is needed and can be calculated following the eq. (5.2). Table 5.1 shows ten inlet velocity values, which are set up in the simulations.

$V_1(m/s)$	3.655	3.883	4.112	4.340	4.569	4.797	5.026	5.254	5.482	5.711
ϕ	0.608	0.646	0.684	0.722	0.760	0.798	0.836	0.874	0.912	0.950

Table 5.1: Inlet velocities according to the flow rate coefficients

$$\phi = \frac{Q}{nD^3} \tag{5.1}$$

$$\psi = \frac{H}{\rho n^2 D^2} \tag{5.2}$$

To obtain a suitable mesh for the AxWJ-2 validation simulation, the investigation of mesh influence is performed by monitoring the impeller torque. While changing the mesh density, the y^+ values are guaranteed to comply with the computational requirements. For the AxWJ-2 validation simulation, the total number of cells is varied from 3.7 x 10^6 up to 5.8 x 10^6 as shown in table 5.2.

	values (x 10^6)					
the total number of cells	3.77	3.94	4.22	4.67	5.56	5.84

Table 5.2: Mesh sensitivity study range for the AxWJ-2 validation simulation

5.2 Validation Results of AxWJ-2 pump

First of all, the mesh quality needs to be checked. Figure 5.3 demonstrates the y^+ values in the rotor and stator regions as the y^+ values must be controlled to have the value less than or around 1 for a wall resolved boundary layer.

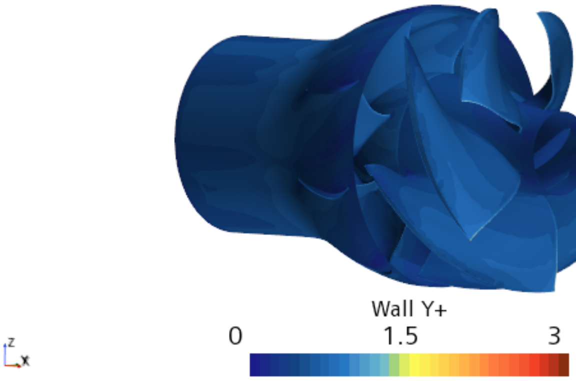

Figure 5.3: y^+ values for the AxWJ-2 pump at $V_1 = 5.711$ m/s

The values between the simulations in STAR CCM+ and the experimental data are compared. The pump performance curve can be shown in fig. 5.4. It presents the relation between head rise (H) and volumetric flow rate (Q). Figure 5.5 compares the values of flow coefficient (ϕ) and head coefficient (ψ). The flow coefficients (ϕ) are scaled with the best flow coefficient (ϕ_{BEP}) of 0.76, while the head coefficients (ψ) are scaled with the best head coefficient (ψ_{BEP}) of 2.46. The values of ϕ_{BEP} and ψ_{BEP} are obtained from the John Hopkins University. According to the plots, it can be seen that the validation is satisfied since the simulation results match remarkably good with the experimental data.

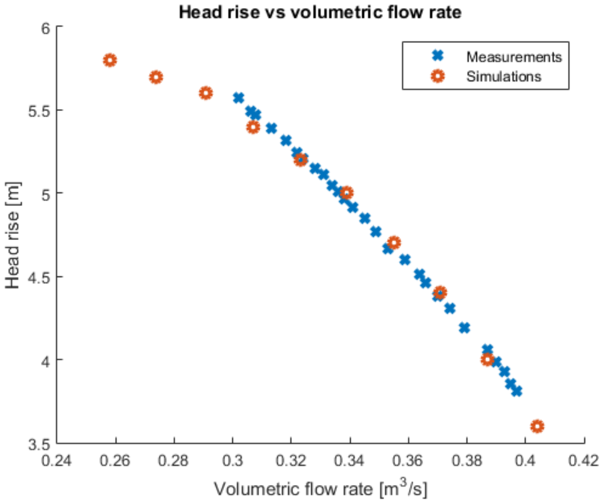

Figure 5.4: Head rise vs volumetric flow rate

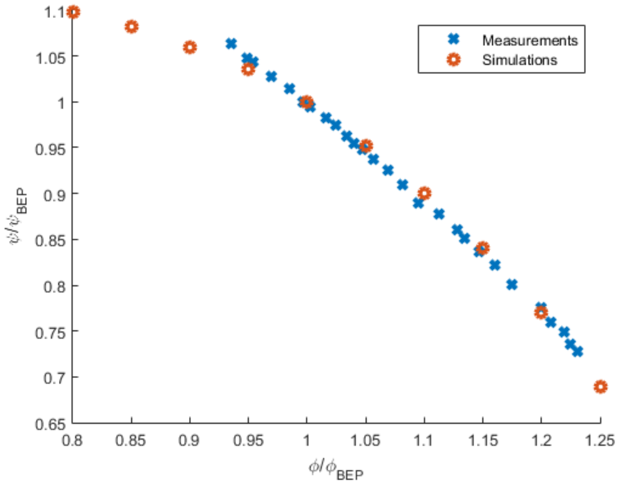

Figure 5.5: Comparison between measured and simulated head coefficient

The pump efficiency can be shown below in fig. 5.6. However, there is no data on torque measurement available from the experiment, so the comparison for the pump efficiency is not performed. Although no torque measurements are available, Thad J et al. (2008) mentions that AxWJ-2 pump is designed to have a maximum efficiency of about 90%. Figure 5.6 shows that the maximum efficiency reaches 89.5%, which matches what the pump designer was aiming for.

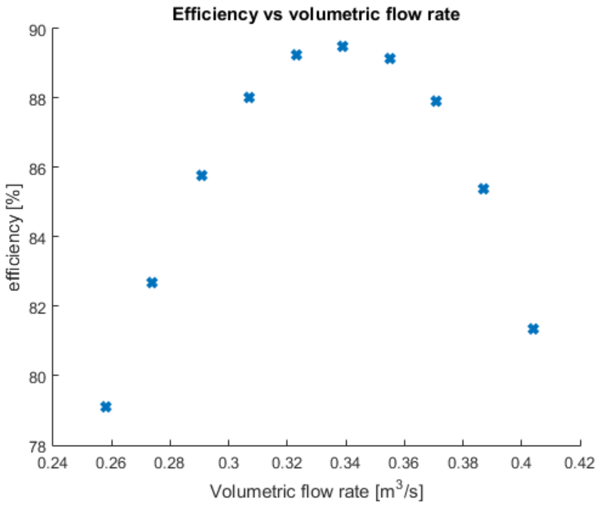

Figure 5.6: efficiency vs volumetric flow rate

According to the mesh sensitivity analysis, figure 5.7 shows the numerical uncertainty study for the AxWJ-2 pump. It contains a refinement ratio ranging from 1 to 1.2. A decent study must cover a refinement ratio range of at least between 1 to 2, while 1 is the finest mesh. Thus, the future project should have increased the refinement steps for a more accurate study. A formal verification based on the Least Squares Root method by Eca L. and Hoekstra (2014) was carried out. The mesh number of 4.6E6 cells shows a good compromise between numerical accuracy and computational effort and was used for the validation study. The numerical uncertainty for this grid was 3.25%.

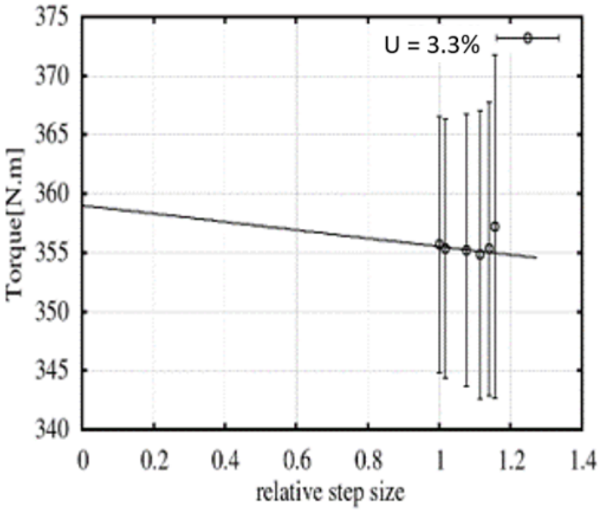

Figure 5.7: numerical uncertainty study for the AxWJ-2 pump

Number of cells (x 10^6)	refinement ratio	Discretization uncertainty (%)
5.84	1.000	3.06
5.56	1.016	3.08
4.67	1.077	3.25
4.22	1.114	3.44
3.94	1.140	3.51
3.77	1.156	4.09

Table 5.3: Discretization uncertainty values for all number of cells (validation study)

6

Optimization Study

6.1 Original intake geometry

After introducing the methodology used to generate the parametric intake model, Table 6.1 represents the initial design parameters to start the investigation. Such parameters are the ones used to generate the metasurface.

parameters	values	units
L	1.441	m
D	0.3048	m
H	0.265	m
α	26	deg
R_2	1.3	m
h_{lip}	0.0375	m
R_3	0.0245	m
beam factor (f_b)	1.5	-
weight top (w_t)	3	-
weight bottom (w_b)	1.2	-
weight top area adjust (f_{area})	1	-
start tangential angle top (θ_t)	45	deg
end tangential angle top	45	deg

Table 6.1: Original intake design parameters

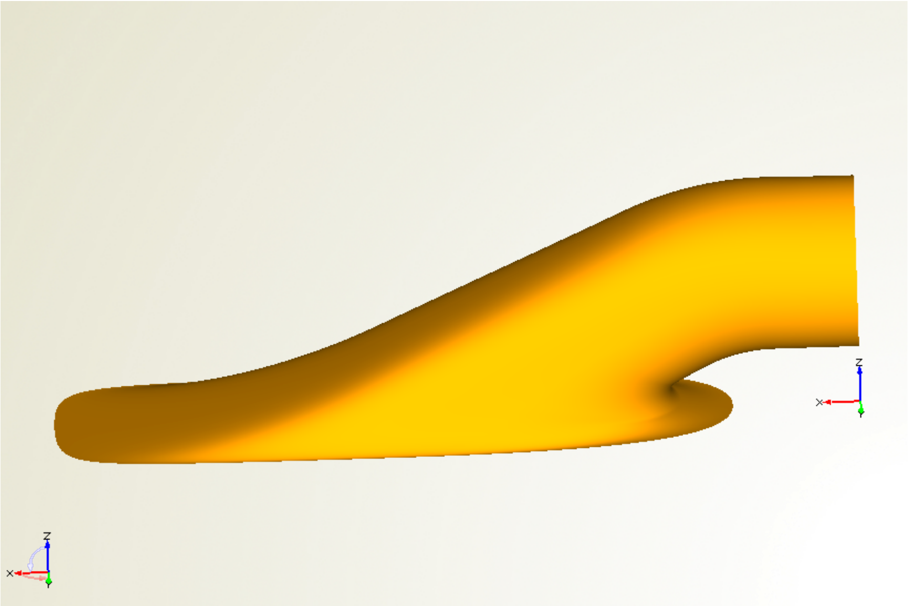

Figure 6.1: Original intake design

6.2 Verification and Mesh sensitivity analysis

Theoretically, the higher number of mesh and grids density, the computation accuracy will generally be improved. However, as the number of grids increases, the computational cost is more expensive. Therefore, the final grid number of the entire computational domain is needed to be determined. To obtain a suitable mesh, the investigation of mesh influence is performed by monitoring the impeller torque. While changing the mesh density, the y^+ values are guaranteed to comply with the computational requirements. For the whole computational domain simulation, the total number of cells is varied from 4.4 x 10^6 up to 7.2 x 10^6 as shown in table 6.2.

	values (x 10^6)					
the total number of cells	4.47	4.68	5.02	5.63	6.02	7.18

Table 6.2: Mesh sensitivity study range for the whole computational domain simulation

Figure 6.2 shows the numerical uncertainty study for the computational domain. It contains a refinement ratio ranging from 1 to 1.2. A decent study must cover a refinement ratio range of at least between 1 to 2, while 1 is the finest mesh. Thus, the future project should have increased the refinement steps for a more accurate study. A formal verification based on the Least Squares Root method by Eca L. and Hoekstra (2014) was carried out. The mesh number of $5.6E6$ cells shows a good compromise between numerical accuracy and computational effort and was used for further studies. The numerical uncertainty for this grid was 3.85%.

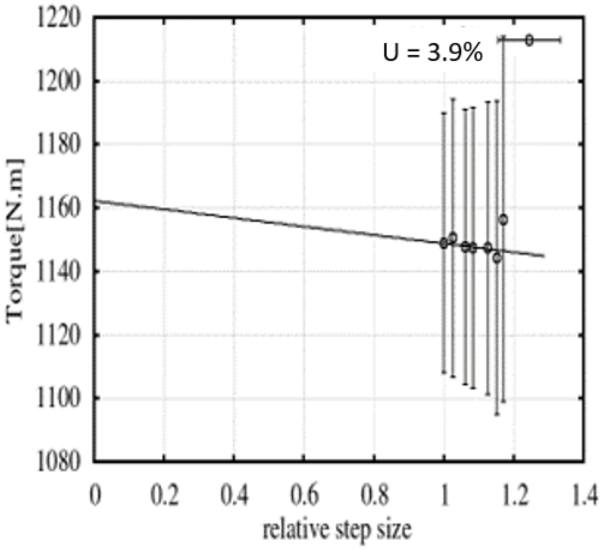

Figure 6.2: numerical uncertainty study for the computational domain

Number of cells (x 10^6)	refinement ratio	Discretization uncertainty (%)
7.18	1.000	3.56
6.02	1.061	3.78
5.63	1.084	3.85
5.02	1.127	4.01
4.68	1.153	4.29
4.47	1.171	5.01

Table 6.3: Discretization uncertainty values for all number of cells (computational domain study)

6.3 System Performance Curve Set up

At the first stage of this study, the system performance curve shall be determined before starting a geometry variation study. Thus, when the geometry variation is performed, the best system operational point is selected. The mass flow rate variation is set at the extended pipe outlet boundary from 561.1 kg/s to 961.9 kg/s. To obtain the smooth system performance curve, eight mass flow rate values are defined. It means that there are eight simulations, which are carried out to obtain the system performance curve. The mass flow rate ranges can be seen in table 6.4 below.

	value (kg/s)							
mass flow rate	561.1	641.3	721.4	761.9	801.6	842.1	881.7	961.9

Table 6.4: mass flow rate variation for finding the system performance curve

The system efficiency is obtained from the ratio between the hydraulic power generated by the pump and the shaft delivered power as shown in eq. (6.4). In order to compute the hydraulic power, eq. (6.2) is applied. The inlet velocity and inlet pressure can be defined from the average values on the capture area surface, while the outlet velocity and outlet pressure can be defined from the average values on the cross section surface at the nozzle exit. Rotational rate of the impeller (ω) is fixed to 2000 rpm and the impeller torque (τ) can be extracted from the simulation, so the shaft delivered power can be computed following eq. (6.3).

$$H = \frac{(p_{out} - p_{capture}) + \frac{\rho}{2}(V_{out}^2 - V_{capture}^2)}{\rho g} \tag{6.1}$$

$$P_{out} = \rho g Q H \tag{6.2}$$

$$P_{in} = \tau\omega \tag{6.3}$$

$$\eta = \frac{P_{out}}{P_{in}} \tag{6.4}$$

6.4 System Performance Curve Results

Firstly, the mesh quality needs to be checked. Figure 6.3 shows the y$^+$ values in the rotor and stator regions, the y$^+$ values must be controlled to have a value less than or around 1. In addition, the y$^+$ values in the intake and hull bottom regions must be controlled above 30 but less than 150 following the wall function criterion, are shown as well in fig. 6.4.

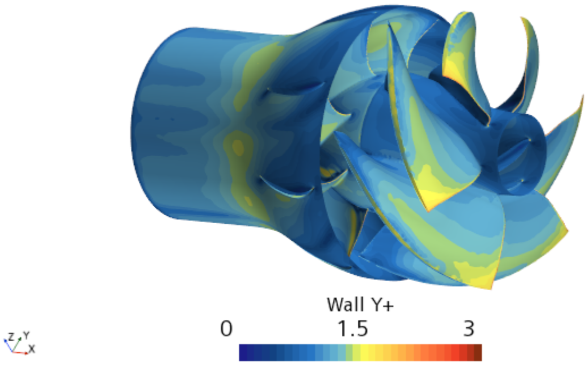

Figure 6.3: y^+ values for the rotor and stator regions at mass flow rate of 961.9 kg/s

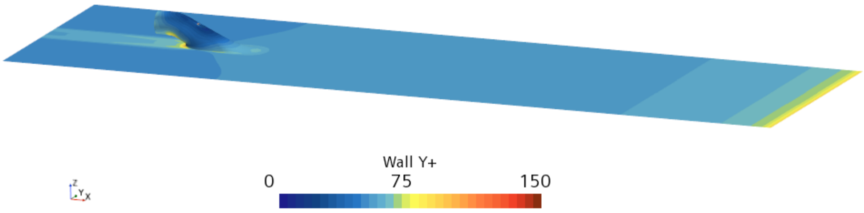

Figure 6.4: y^+ values for the intake and hull bottom regions at mass flow rate of 961.9 kg/s

Figure 6.5 presents the system efficiency curve obtained from eq. (6.4) and head rise curve obtained from eq. (6.1). The curve shows that the system will have the highest efficiency when operating at the mass flow rate of 761.9 kg/s. The maximum efficiency is found to be 72.44%.

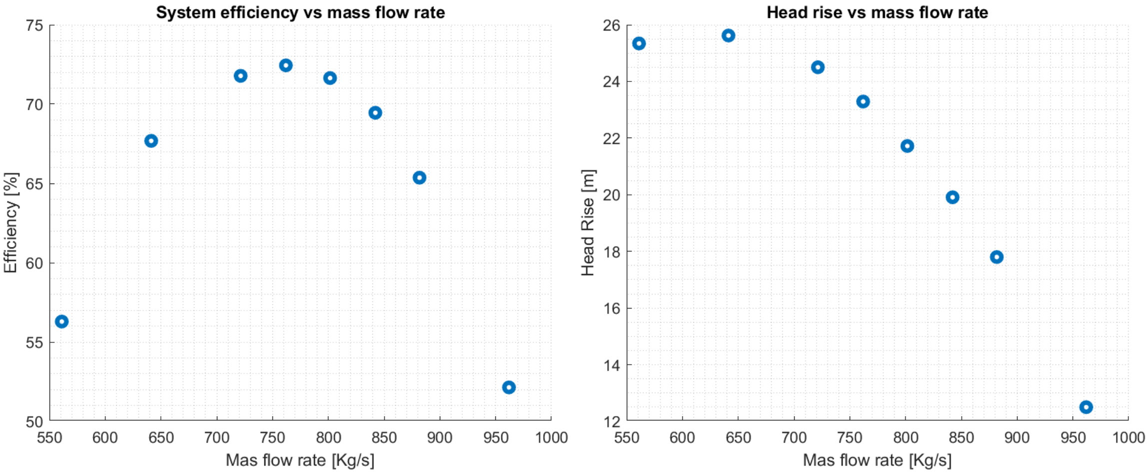

(a) system efficiency vs mass flow rate **(b)** head rise vs mass flow rate

Figure 6.5: System performance curves

To verify the stator performance, the impeller and stator torques are plotted together in fig. 6.6. It shows that the stator performs an excellent function in reducing the flow's swirl motion as the torque produced by the stator has a value close to the impeller torque but in the opposite direction. The impeller and stator torque ratio is close to 1 when the mass flow rate is 761.9 kg/s. This supports the result of the highest efficiency as the loss from swirl motion is reduced significantly by the stator at this mass flow rate.

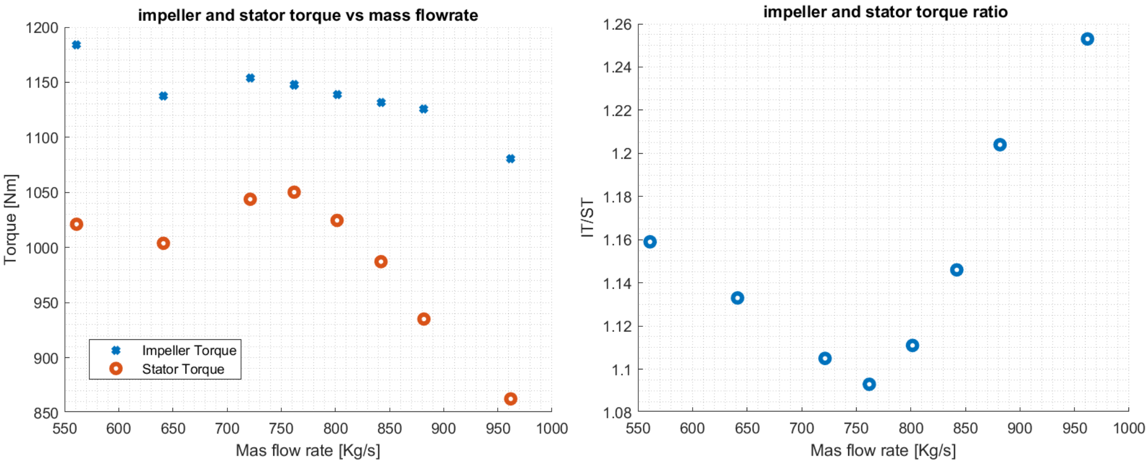

(a) impeller and stator torque vs mass flow rate (sign negligible) **(b)** the ratio between impeller and stator torque

Figure 6.6: Comparison between impeller and stator torque

In this section, the capture areas from eight different mass flow rates are shown in fig 6.7. The capture area is larger when the mass flow rate is higher because more flow is pulled into the intake. Figure 6.8 depicts the streamtube for the mass flow rate of 761.9 kg/s which is obtained from the capture area extraction procedure as mentioned in section 4.4.

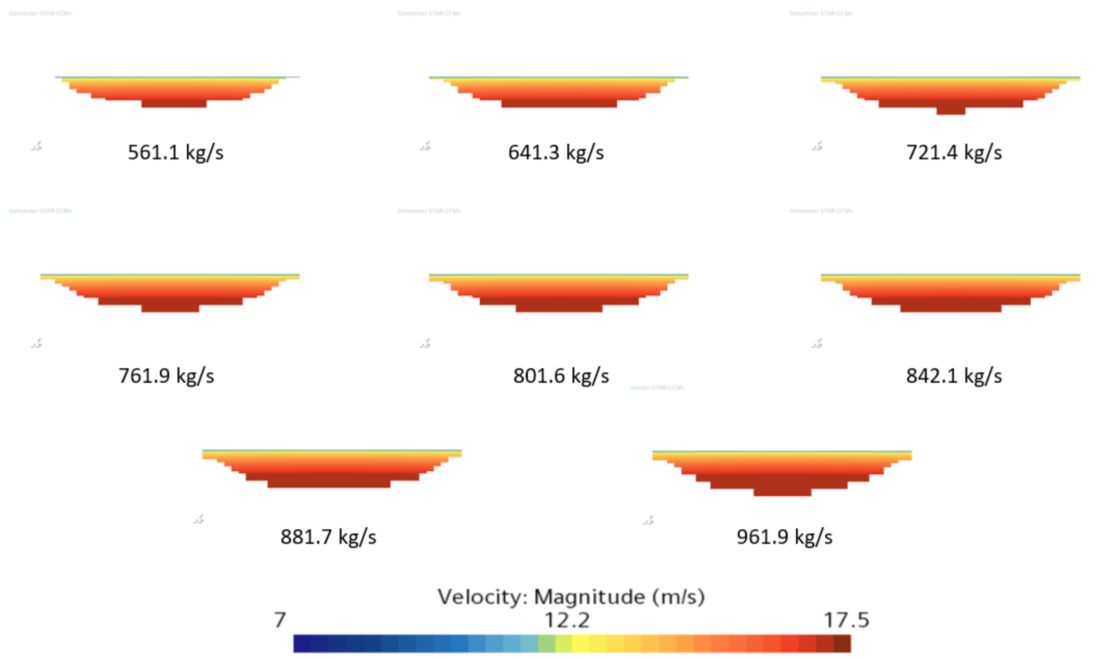

Figure 6.7: Capture area from eight different mass flow rates

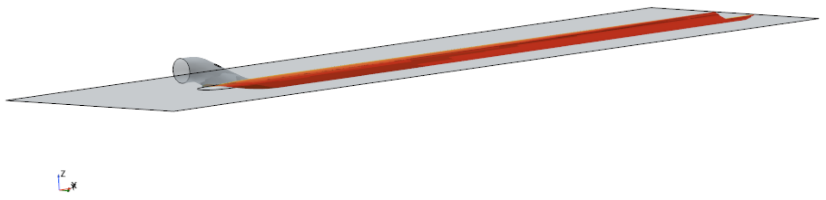

Figure 6.8: streamtube at mass flow rate of 761.9 kg/s

One phenomenon that can be observed when studying the system performance curve is flow separation. From the mass conservation rule, the higher the mass flow rate, the faster fluid flow will be. Separation occurs when the fluid velocity in the duct is lower than a certain value and affects the whole system performance. This obviously happens with low mass flow rates such as 561.1 ks/s and 641.3 kg/s. As shown in fig. 6.9, the separation occurs at the top of the intake ramp region because the velocity there is low enough and cannot overcome the adverse pressure gradient.

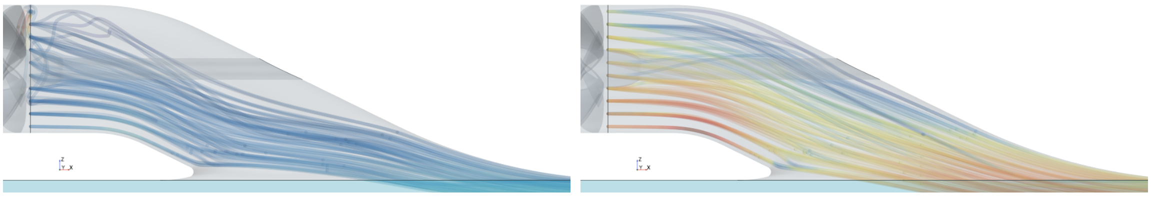

(a) 561.1 kg/s **(b)** 961.9 kg/s

Figure 6.9: Streamline for the mass flow rate of 561.1 kg/s and 961.9 kg/s

6.5 Extending Pump-Intake Connection Set up

Before starting optimization, it is good to understand the general physics of the system. There are two parameters that might help to increase the system efficiency. First is the surface uniformity of the axial velocity at the pump upstream cross section, which can be called as a pump inflow uniformity. This pump upstream cross section is located at $0.1D$ before the pump inlet surface (Siemens, 2018). The pump should operate more effectively if the inlet axial velocity of the fluid is more uniform. This helps to reduce the non-uniform blade loading problem and is good for noise and vibration reduction. The pump inflow uniformity can be defined by the following eq. (6.5). The second parameter is the flow perpendicularity at the pump upstream cross section. It can be said that the pump can operate more efficiently when the axial component of the flow velocity is as high as possible compared to its magnitude. This can be explained as follows: if the flow is not perfectly perpendicular to the cross section plane, this can affect the blade's angle of attack. The perpendicularity parameter can be defined by the following eq. (6.6).

$$\xi_{v_a} = 1 - [\frac{\sum_f |V_{a,f} - \overline{V_a}| A_f}{2|\overline{V_a}| \sum_f A_f}] \tag{6.5}$$

$$\phi_p = \frac{1}{Q} \int_{dA} V_a [90^\circ - \arctan(\frac{V_t}{V_a})] dA \tag{6.6}$$

From eq. (6.5), it can be seen that the surface uniformity of the axial velocity is good if this value is close to 1. If the quantity is distributed equally, the resulting number is 1 (Siemens, 2018). From eq. (6.6), if the perpendicularity is equal to 90, it means that the flow is perfectly perpendicular to the cross section plane. Thus, it is good to have this resulting number as close to 90 as possible (Huang et al., 2019).

In order to verify this hypothesis, the extending pump-intake connection study has been carried out. During this study, the mass flow rate is fixed at 761.9 kg/s, which is the best system operating point obtained from the system performance study. The pump-intake connection is basically the circular pipe that connects the intake to the pump. In the original geometry, the pump is connected directly to the intake. The pump-intake connection length variation is set from 0 to $4D$. Furthermore, one additional simulation is performed to have a better understanding of these parameters. For this extra one, the intake is removed and there is a long straight pipe with a length of $10D$ before the pump inlet as shown in fig. 6.12. It is assumed to be the best working operational condition for the pump because the intake is actually the main reason for non-perpendicularity and non-uniform flow. The intake connection length ranges can be seen in table 6.5 below.

	value (m)					
	with intake					without intake
intake connection length	0	0.3	0.6	0.9	1.2	3

Table 6.5: pump-intake connection length variation

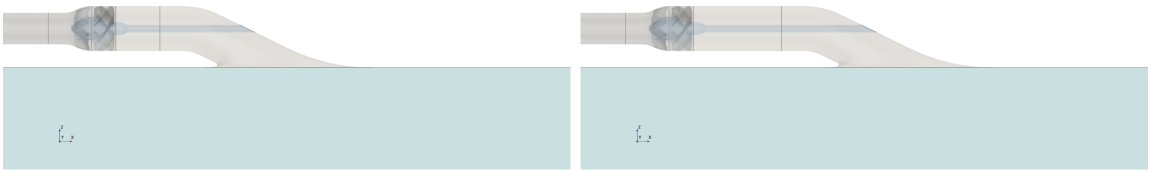

(a) intake connection length = 0.3 m **(b)** intake connection length = 0.6 m

Figure 6.10: Pump-Intake connection length variation

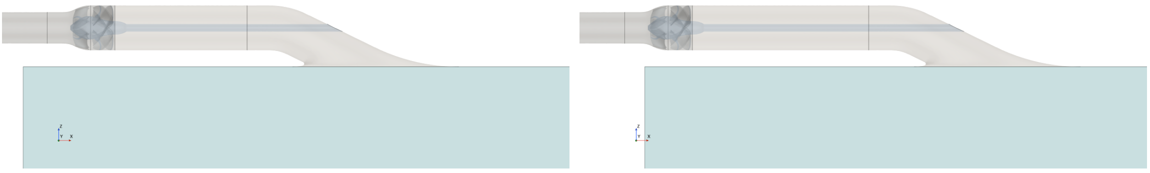

(a) intake connection length = 0.9 m **(b)** intake connection length = 1.2 m

Figure 6.11: Pump-Intake connection length variation

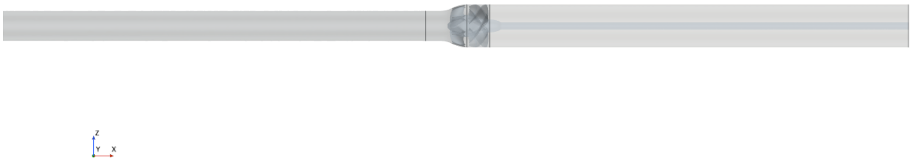

Figure 6.12: Without intake setup

6.6 Extending Pump-Intake Connection Results

Figure 6.13 shows the intake connection study results in terms of efficiency. The efficiency increases gradually when the intake connection is extended. Moreover, it can be seen that the thrust-over-torque parameter, which is mentioned in section 6.11.1 can be used to represent the trend of the system efficiency when the intake geometry is changed. As expected, the longer the intake connection, the inflow to the pump is better for both pump inflow uniformity and perpendicularity, as shown in fig 6.14. This also results in lower torque and higher thrust summation when the intake connection length is longer, as shown in fig. 6.15. However, there is a limit to this efficiency increase when extending the intake connection because the inflow is better, but the friction loss in the intake connection part is larger as well. Thus, at a certain point, the friction loss overcomes the benefit of a more uniform inflow.

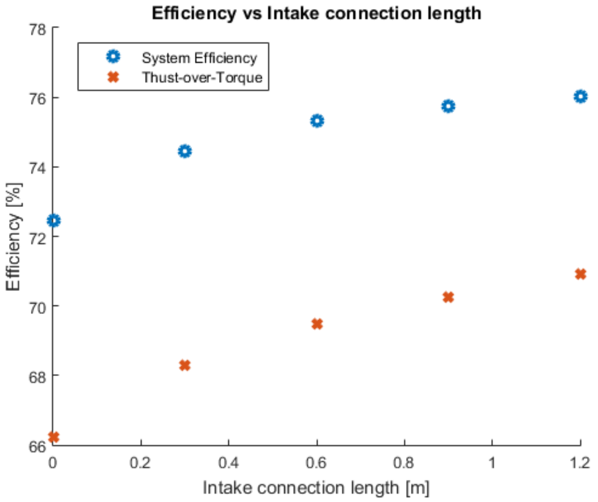

Figure 6.13: Efficiency vs intake connection length

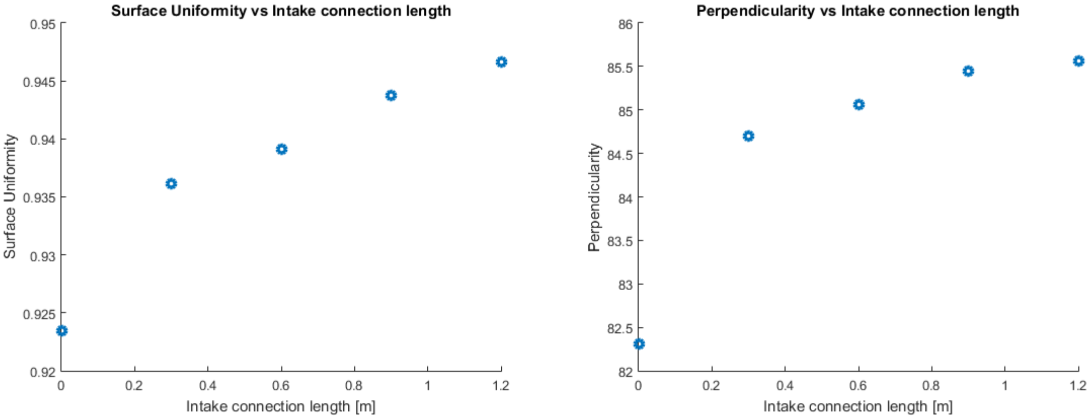

(a) Pump Inflow Uniformity vs intake connection length

(b) Perpendicularity vs intake connection length

Figure 6.14: Pump Inflow Uniformity and Perpendicularity vs intake connection length

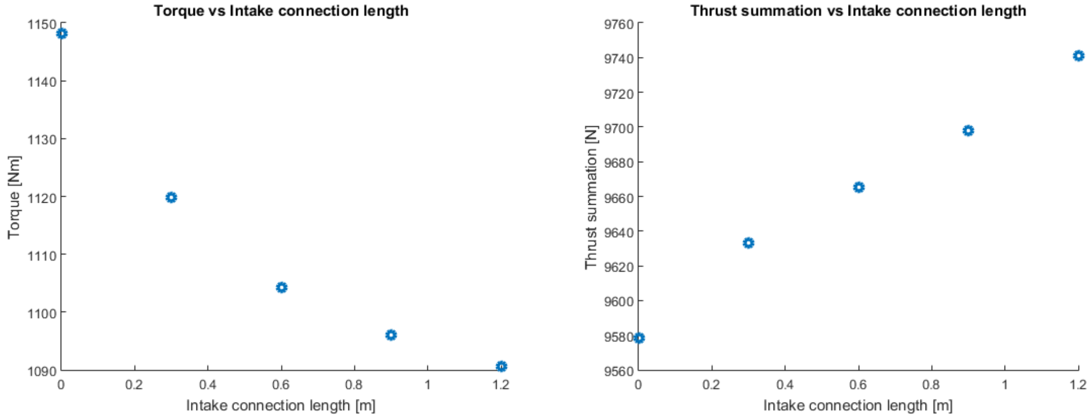

(a) Torque vs intake connection length

(b) Thrust Summation vs intake connection length

Figure 6.15: Thrust and Torque vs intake connection length

Table 6.6 depicts the results from the simulation without intake setup. The efficiency can reach 90.5%. This is extremely high. It also matches the pump designer's aim because this pump is designed to have a maximum efficiency of about 90% in the horizontal domain. The physical quantities also support the study, including the higher pump inflow uniformity, higher perpendicularity, and lower torque.

parameters	values	units
efficiency	90.5	%
surface uniformity	0.968	-
perpendicularity	86.88	deg
torque	971.3	Nm

Table 6.6: Without intake setup results

The axial velocity profile at the pump upstream cross section can be extracted as shown in fig. 6.16. The inflow to the pump is more uniform when the intake connection is longer. Because of the intake shape, it results in a higher velocity at the bottom and a lower velocity at the top. However, this is not the case for the without intake setup as there is no upward movement of the flow, so the inflow to the pump is remarkably uniform compared to with intake simulations. As the shaft is rotating in the counter clockwise direction and the flow is moving upward when passing through the intake, the axial velocity is lower near the shaft line on the left side because the shaft rotation motion and the flow motion are in different directions.

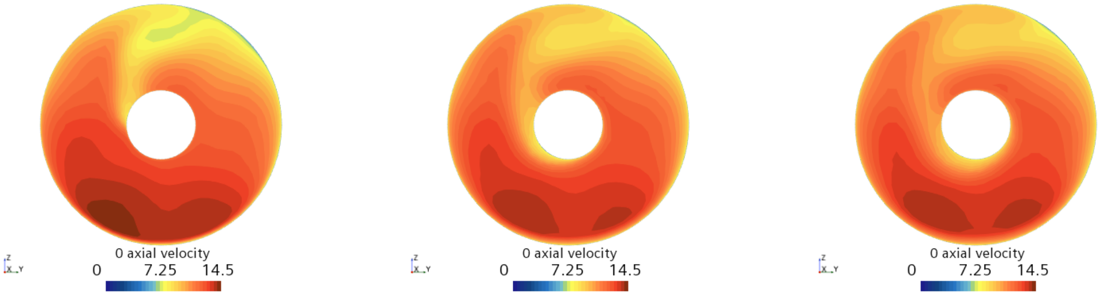

(a) length = 0 m **(b)** length = 0.3 m **(c)** length = 0.6 m

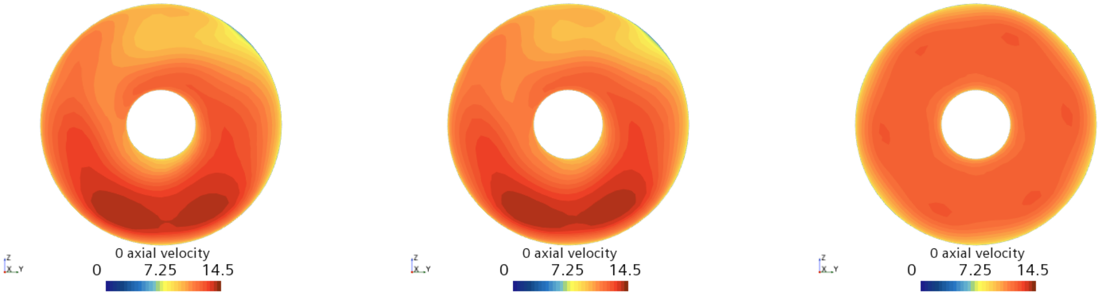

(d) length = 0.9 m **(e)** length = 1.2 m **(f)** length = 3 m (without intake)

Figure 6.16: axial velocity vs intake connection length

To observe the inflow quality to the pump, the ratio of the tangential velocity and axial velocity (V_t/V_a) can be used. The lower this ratio, the better inflow quality to the pump is obtained as the tangential velocity will normally degrade the pump performance. V_t/V_a profile at the pump upstream cross section can be extracted as shown in fig. 6.17. The tangential velocity component is generated due to the shaft rotation and the intake shape. Thus, it can be seen that V_t/V_a is remarkably low in the without intake setup case.

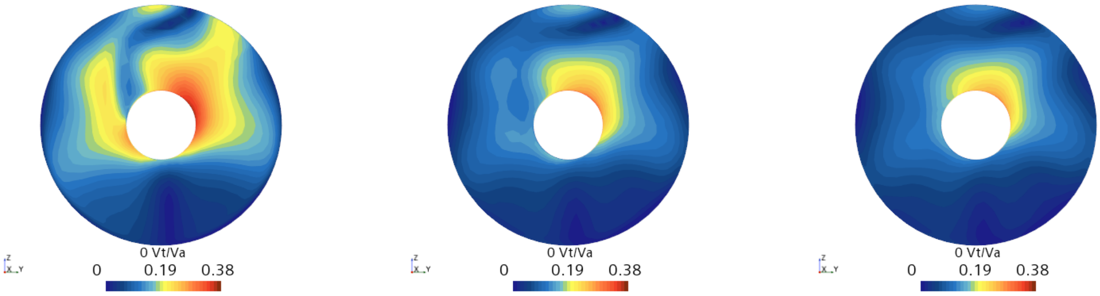

(a) length = 0 m **(b)** length = 0.3 m **(c)** length = 0.6 m

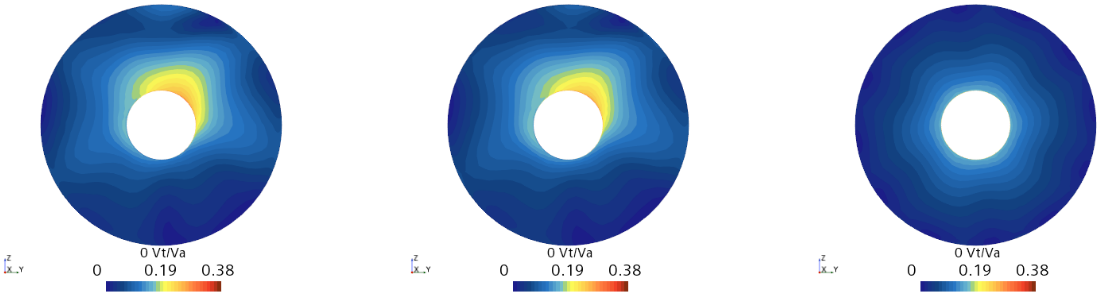

(d) length = 0.9 m **(e)** length = 1.2 m **(f)** length = 3 m (without intake)

Figure 6.17: V_t/V_a vs intake connection length

6.7 Shaft Removal Set up

Nowadays, electric propulsion has been developed worldwide. This allows the possibility to do more research on how it can affect the hydrodynamic performance of the waterjet propulsion system. With electric propulsion, one can think of employing a rim-driven pump instead of driving it with a shaft line. This may also reduce the nonuniform flow into the pump, which is good for the pump's performance. This section will study the effects of the shaft removal condition compared to the shaft-existing condition. The eight simulations, which varied eight mass flow rates as before, are repeated. The computational domain is modified by removing the shaft and adding the impeller hub tip as shown in fig. 6.19. This section is just for educational purposes, so it might not work in practice, as it is assumed that the motor can be fitted inside the impeller hub. The pump housing in the rotor region is not moving, similar to the previous simulation.

Figure 6.18: absence of shaft simulation domain

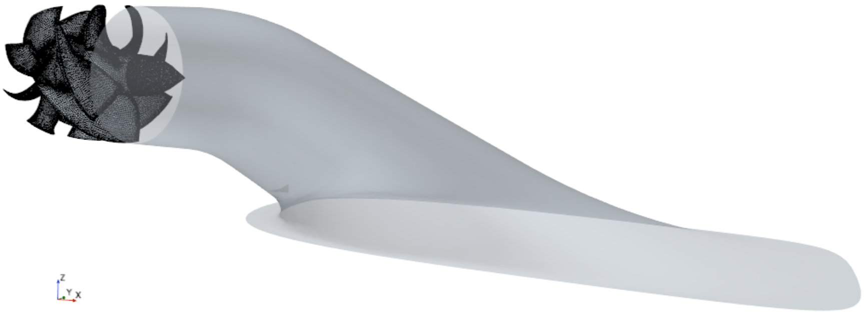

Figure 6.19: absence of shaft simulation domain (perspective view)

6.8 Shaft Removal Results

The performance of all mass flow rate conditions for both shaft-existing and shaft removal conditions are shown in this section. As shown in fig. 6.20, the system efficiency for the shaft removal condition is a little bit higher than the shaft-existing condition for most cases except the mass flow rate of 641.3 kg/s. Looking at efficiency, there is no large difference. However, the trust summation for the shaft removal condition is significantly higher than the shaft-existing condition for most cases. Although the thrust is higher, the torque is also higher, as shown in fig 6.21. This is the reason why the efficiency does not change much in the end.

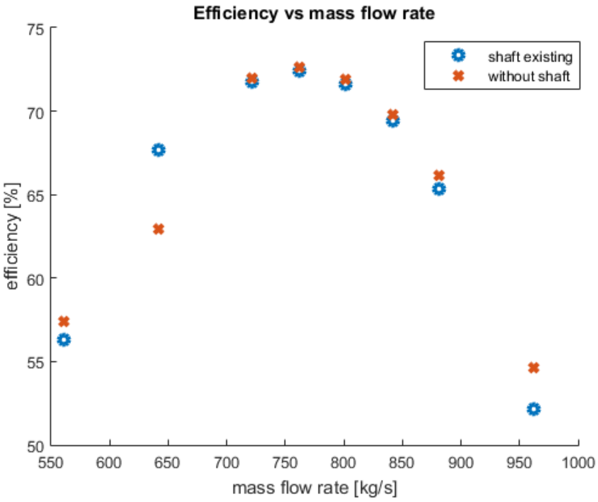

Figure 6.20: Efficiency vs mass flow rate between shaft-existing and shaft removal

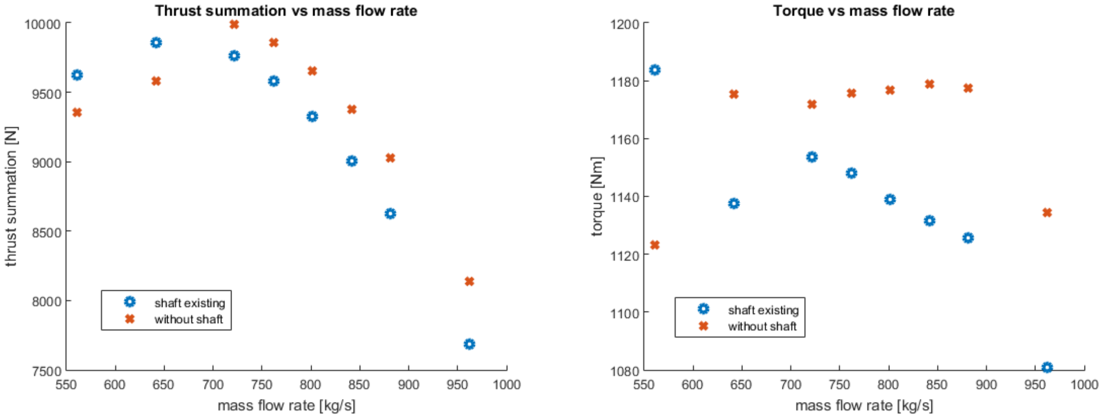

(a) Thrust summation vs mass flow rate **(b)** Torque vs mass flow rate

Figure 6.21: Torque and Thrust vs mass flow rate between shaft-existing and shaft removal

To support the results, the head plot between the shaft-existing and shaft removal conditions for the mass flow rate of 801.6 kg/s along the longitudinal position is shown in fig. 6.22. The intake end cross section, which is attached to the rotor region, is located at x = 0 m. The intake has the length about 1.4 m, so the capture area cross section is located at x = 1.7 m. According to the plot, the head generated by the impeller for the shaft removal condition is higher than the shaft-existing condition. It results in a higher thrust summation as mentioned before.

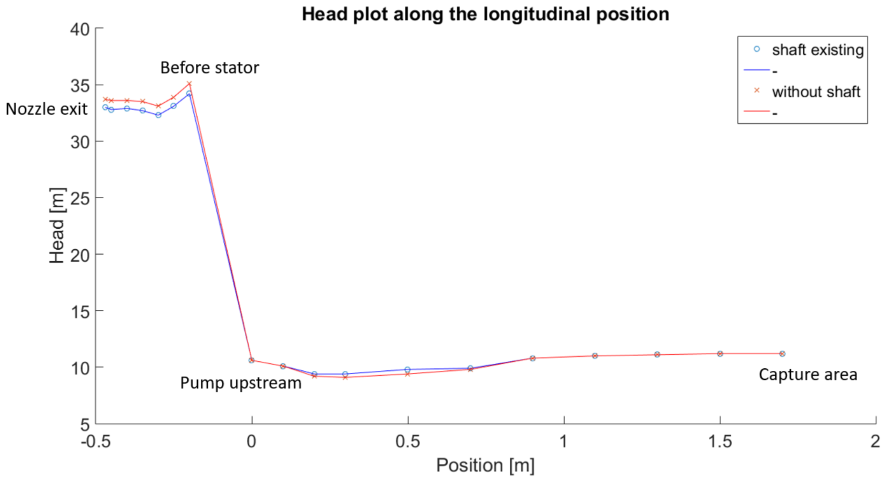

Figure 6.22: Head plot vs longitudinal position between shaft existing and without shaft conditions at 801.6 kg/s

The axial velocity at the pump upstream cross section comparison between the shaft-existing and shaft removal conditions for the mass flow rate of 761.9 kg/s is presented in fig. 6.23. The wake fields for both conditions are different because of the shaft rotation effect. The different wake field can induce different angle of attack on the blades and results in different thrust.

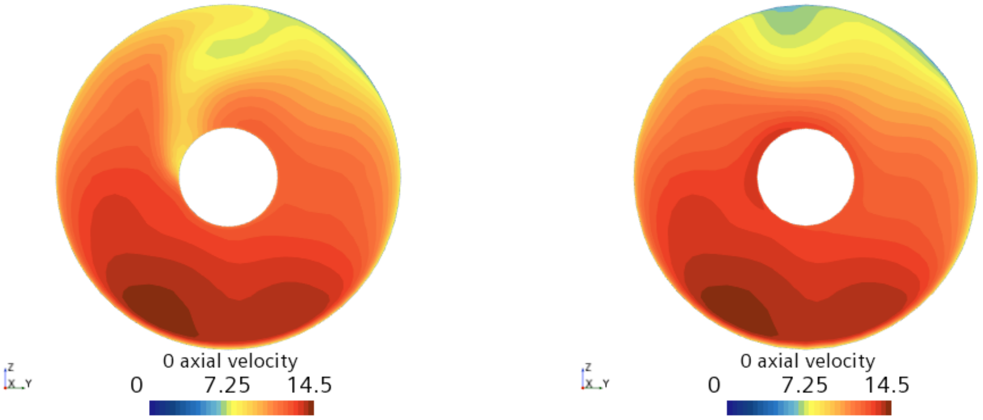

(a) Shaft existing **(b)** Without shaft

Figure 6.23: Axial velocity at the pump upstream cross section comparison between shaft-existing and shaft removal

V_t/V_a at the pump upstream cross section comparison between the shaft-existing and shaft removal conditions for the mass flow rate of 761.9 kg/s is depicted in fig. 6.24. the inflow to the pump between both conditions is different and results in different pump performance. Even though the efficiencies are quite similar, the thrust generated by the shaft removal condition is higher. At this stage, it can be said that the angle of attack for the shaft removal condition is higher than the shaft-existing condition.

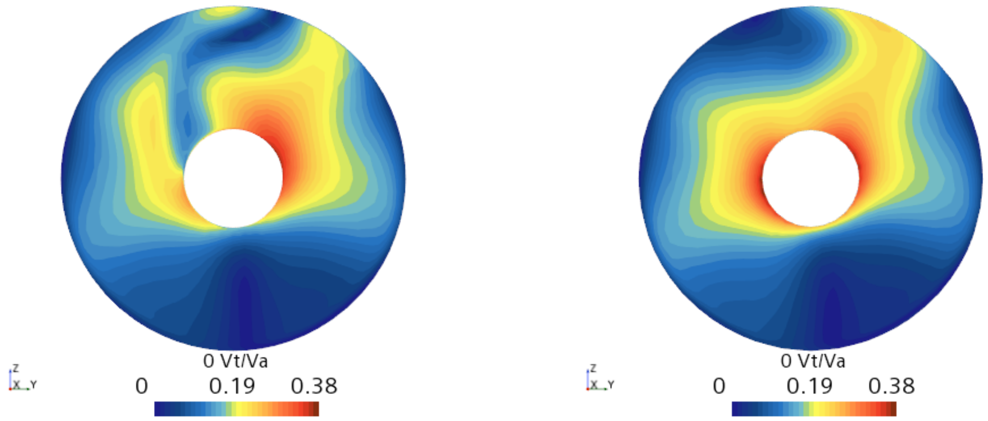

(a) Shaft existing **(b)** Without shaft

Figure 6.24: V_t/V_a at the pump upstream cross section comparison between shaft-existing and shaft removal

The tip leakage phenomenon can be detected easily with a mass flow rate of 641.3 kg/s. Figure 6.25 shows the axial velocity contour. At the top of the section, the backward flow can be seen with a blue color because of the tip leakage phenomenon. This phenomenon can degrade the efficiency of the entire system and can be observed obviously when the pressure difference between the pressure side and the suction side of the pump is large. It can be seen that the position where the tip leakage occurs appears at the same position where the pressure on the suction side is extremely low, while the pressure on the pressure side is quite high, as shown in fig. 6.26.

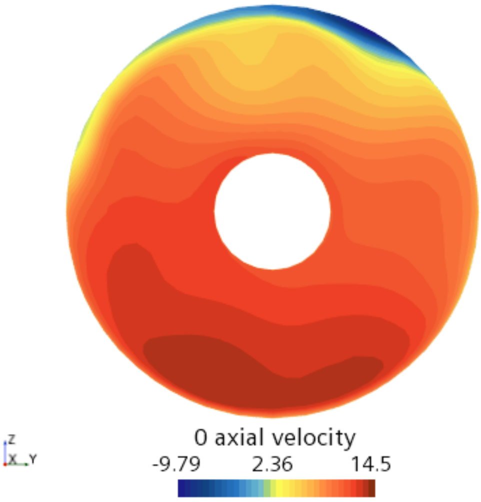

Figure 6.25: Axial velocity field at the pump upstream cross section for the mass flow rate of 641.3 kg/s

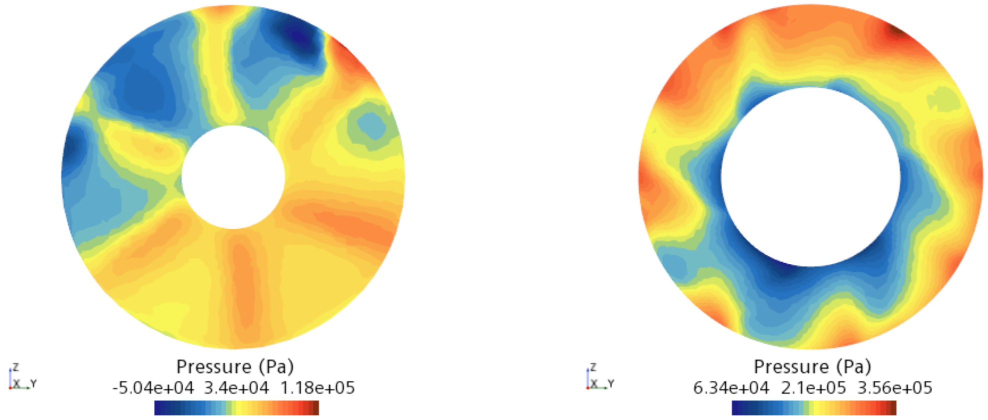

(a) Suction side

(b) Pressure side

Figure 6.26: Pressure contour plot of the mass flow rate of 641.3 kg/s

Figure 6.27 presents the head plot along the longitudinal position of three different mass flow rates. It can be seen that the pressure difference for the mass flow rate of 561.1 kg/s is much larger than others. Thus, the tip leakage phenomenon tends to occur more easily when the waterjet operates in the low mass flow rate range.

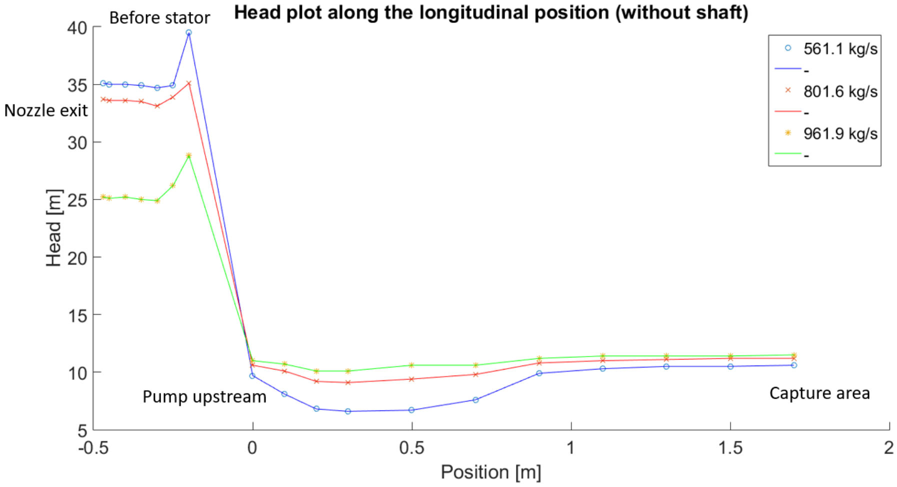

Figure 6.27: Head plot vs longitudinal position with different mass flow rate conditions

6.9 Rim-driven Impeller Set up

As the effect of shaft removal is investigated in the section 6.7, the rim-driven impeller is introduced in this section. The impeller hub is still in the same position. However, the rotor is modified a little bit by closing the tip gap between the blade tip and the pump housing as shown in fig. 6.28. Now, the pump housing has to be rotated as the pump is rotated by a rim-driven mechanism. Therefore, the pump housing's relative motion is removed.

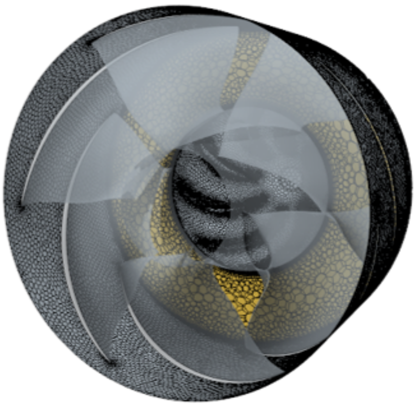

Figure 6.28: Rim driven pump (no tip gap)

6.10 Rim-driven Impeller Results

Fig. 6.29 presents the efficiency for each mass flow rate comparison between having a tip gap and no tip gap conditions. The system efficiency of the studies pump without a tip gap is significantly lower than having a tip gap. Although the thrust summation values are quite similar for both conditions, torque values are remarkably different, as shown in fig. 6.30. It is observed that the pump housing in the rotor region is the main reason. Because it is rotating in the rim-driven case, higher torque is needed to rotate this housing apart from the impeller, which results in the larger delivered shaft power demanded.

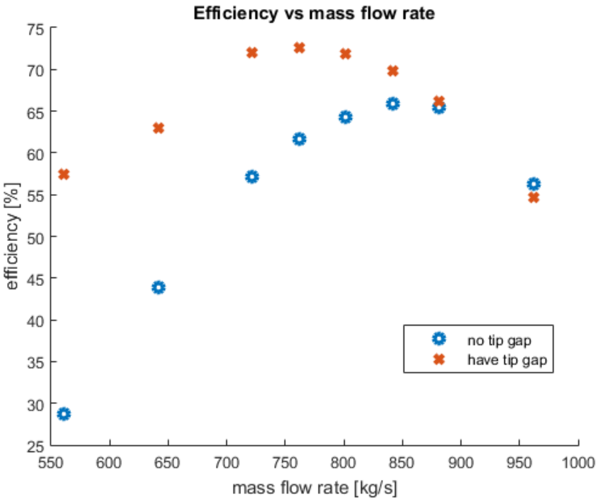

Figure 6.29: Efficiency vs mass flow rate between having tip gap and no tip gap

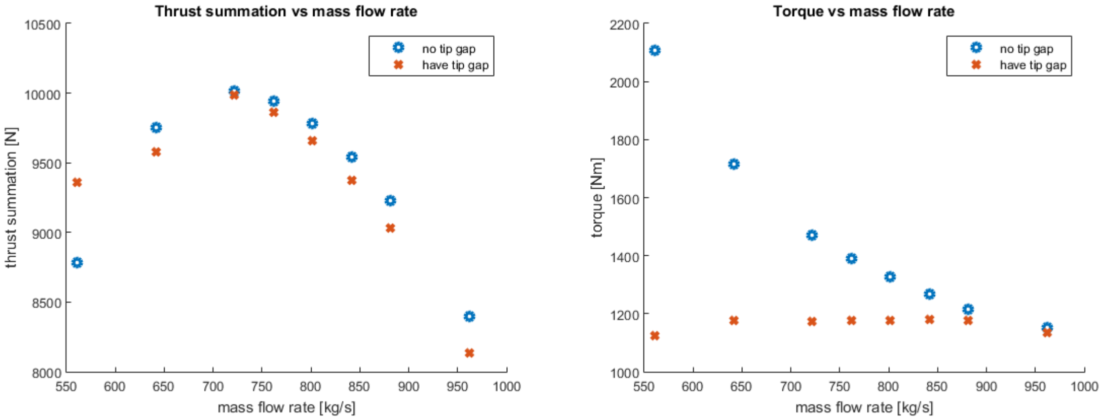

(a) Thrust summation vs mass flow rate **(b)** Torque vs mass flow rate

Figure 6.30: Torque and Thrust vs mass flow rate between having tip gap and no tip gap

The difference between both conditions is the tip clearance, so everything apart from that is still the same. Thus, the inflow to the pump remains similar as shown in fig. 6.31 and 6.32. However, the behavior is different when the fluid enters the pump region. Figure 6.33 shows the V_t/V_a field at the stator start cross section comparison between having a tip gap and no tip gap. This cross section is found where the flow enters the stator region after passing the impeller. It is evident that the contour plots are different near the pump housing. Due to the housing rotation, the tangential velocity component is high there, making the red color zone on the wall easily visible.

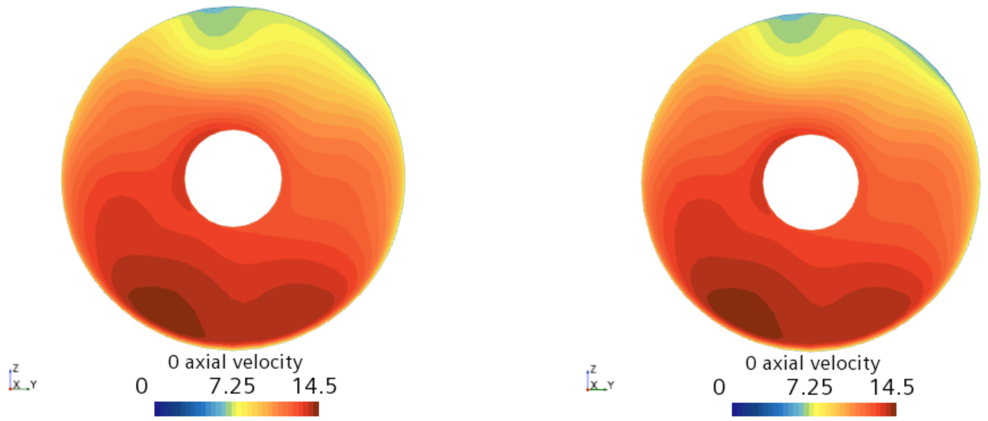

(a) having tip gap **(b)** no tip gap

Figure 6.31: Axial velocity field at the pump upstream cross section comparison between having tip gap and no tip gap

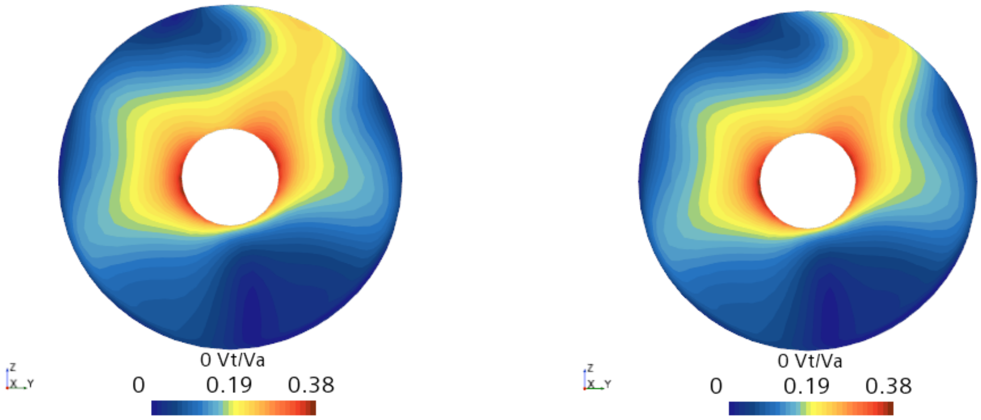

(a) having tip gap **(b)** no tip gap

Figure 6.32: V_t/V_a at the pump upstream cross section comparison between having tip gap and no tip gap

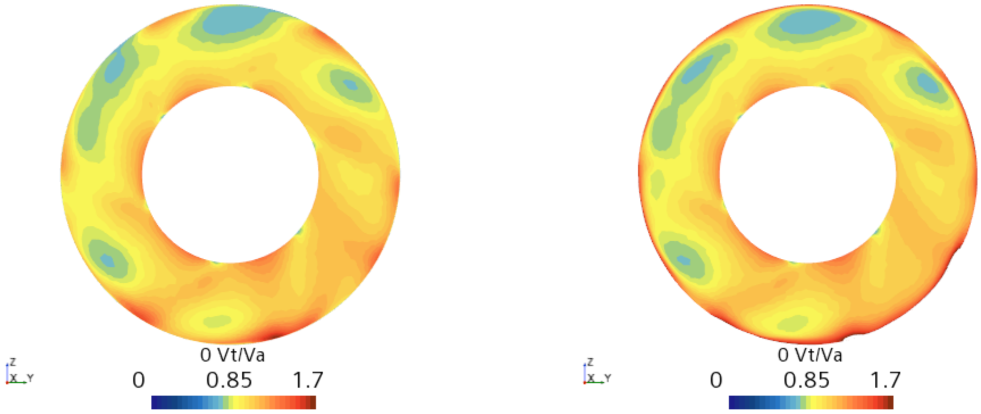

(a) having tip gap **(b)** no tip gap

Figure 6.33: V_t/V_a at the stator start cross section comparison between having tip gap and no tip gap

6.11 Intake Optimization Set up

An optimization procedure can be done in CAESES as it has a DAKOTA tool plug-in, which can perform the optimization investigation based on the response surface method. Due to the optimization computation requirements, simulations must be run on a cluster. CAESES is already coupled with STAR CCM+ as mentioned in section 4.5, so the only thing left here is to find a way to execute CAESES in batch mode, so the geometry variation is taken into account and the optimization can be performed on Linux. Fortunately, it is simple to execute CAESES on Linux because the only things that need to be written in the script are the geometry variation setup and the command to run the engine. The script can be found in the appendix.

6.11.1 Objective definition

Before running the optimization, an objective has to be defined. Normally, the objective should be the entire system efficiency, which is described in section 6.3. However, the capture extraction is an obstacle here because there is no automated way to perform it yet. It has to be done manually as mentioned in section 4.4. Thus, the entire system efficiency cannot be used. The new objective is introduced, which is the thrust-over-torque parameter. the idea is that thrust, which is created by all components in the system including impeller, stator, casing, and intake can represent the power output when times with the ship speed. The thrust summation can be computed following eq. (6.7), while the thrust -over-torque parameter can be determined following eq. (6.8). To prove this hypothesis, the trends between the entire system efficiency and the thrust-over-torque parameter are plotted in the intake connection study as mentioned in section 6.6, when the intake connection length is varied and the mass flow is constant. The trends are pretty similar, so this parameter can be used as an indicator. later on, after obtaining the best intake shape, the entire system efficiency will be taken into account for a real comparison with the original one.

$$T_{sum} = T_{impeller} + T_{stator} + T_{intake} + T_{casing} \tag{6.7}$$

$$T/\tau = \frac{T_{sum} V_s}{\tau \omega} \tag{6.8}$$

6.11.2 Intake height

After obtaining the basic idea and knowledge of the waterjets' entire system from many investigations, intake optimization can now be carried out. The most significant parameter, which affects the entire performance, is the intake height. The lower intake height is expected to give better efficiency than the higher one because of two main reasons. Firstly, the inflow to the pump should be better, including more uniform and perpendicular, as there is less vertical momentum needed. Secondly, the duct loss should be lower because less energy is demanded to lift the flow upward. Normally, the installation of waterjet propulsion units and their intake design is constrained by the size of the engine and the gearbox. However, the intake height can be varied and not be constrained as the possibility of an electric waterjet is introduced in this project. During the investigation, the intake height varies from 0.21 m to 0.29 m. A smaller intake height than 0.21 m cannot be produced due to CAD design restrictions.

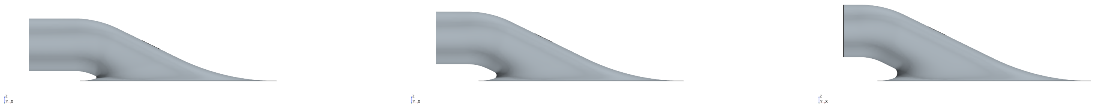

(a) Height = 0.21 m **(b)** Height = 0.25 m **(c)** Height = 0.29 m

Figure 6.34: Intake height variation

6.11.3 Cross section

Many parameters can be changed as inputs in this intake model such as the slope angle (α), ramp radius (R_2), beam factor (f_b), weight bottom (w_b) and weight top (w_t). The intake cross section variation is performed for this project because many studies had already optimized profile intake features such as Weixuan Jiao et al. (2019) and Huang et al. (2019). However, how the cross section variation influences the system efficiency has not been studied in detail yet. After obtaining the best intake height, the cross section optimization can be investigated. Three parameters are selected to run the cross section optimization study, including start tangential angle (θ_t), weight top (w_t), and area adjust factor (f_{area}). Section 4.1.2 defines the meaning of all these parameters. As shown below, fig. 6.35, fig. 6.36, and fig. 6.37 depict how each parameter will affect the shape of the intake.

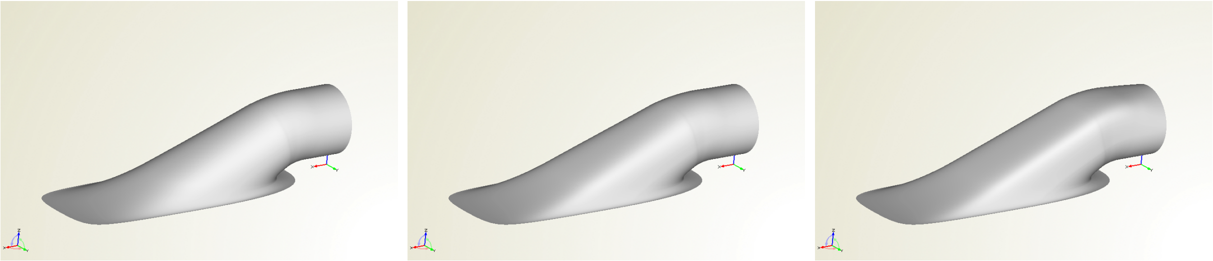

(a) $\theta_t = 0°$ **(b)** $\theta_t = 45°$ **(c)** $\theta_t = 90°$

Figure 6.35: Effect of start tangential angle (θ_t), while $w_t = 3$ and $f_{area} = 1$

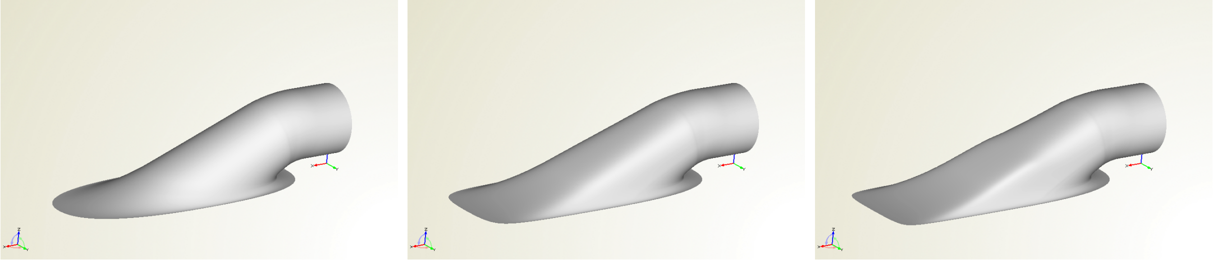

(a) $w_t = 1$ **(b)** $w_t = 3$ **(c)** $w_t = 5$

Figure 6.36: Effect of weight top (w_t), while $\theta_t = 45°$ and $f_{area} = 1$

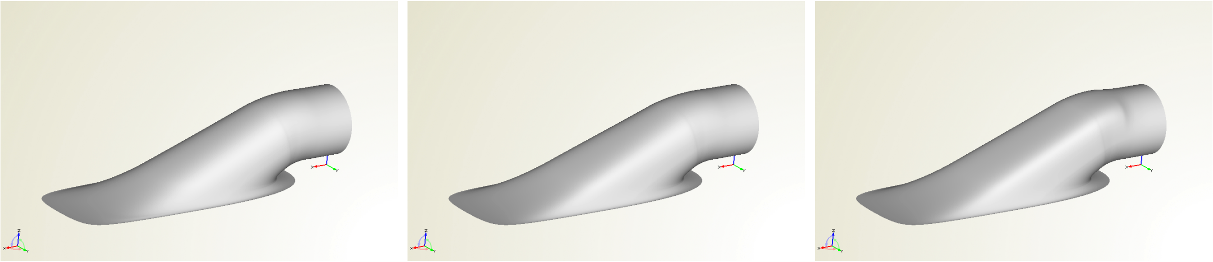

(a) $f_{area} = 0.8$ **(b)** $f_{area} = 1$ **(c)** $f_{area} = 1.2$

Figure 6.37: Effect of area adjust factor (f_{area}), while $\theta_t = 45°$ and $w_t = 3$

6.12 Intake Optimization Results

In this section, the optimization results are shown starting from the intake height optimization. After the best intake height is chosen, the cross section optimization is performed. Finally, the effect of shaft removal on the pump efficiency is studied in the best design.

6.12.1 Intake height

As expected, the lowest intake height gives the best efficiency in terms of thrust-over-torque. The trend is obvious as shown in fig. 6.38. The efficiency for the height of 0.21 m is higher than the height of 0.29 m by approximately 5%, which is quite significant. Thus, the intake height of 0.21 m is selected for study in cross section optimization.

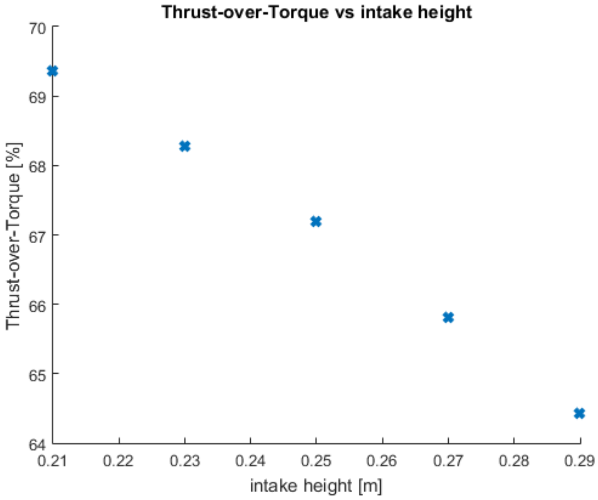

Figure 6.38: Thrust-over-Torque vs intake height

Surface uniformity and perpendicularity are proper indicators to assess the pump efficiency as they give a trend that is similar to the efficiency trend as shown in fig. 6.39. the lowest intake height has the best surface uniformity and perpendicularity values. The lower the intake height, the vertical movement of the flow is reduced and resulting in a better inflow to the pump. Moreover, the shaft wake disturbs the flow to the pump less when the intake flow has a smaller non-axial component (more aligned with the shaft).

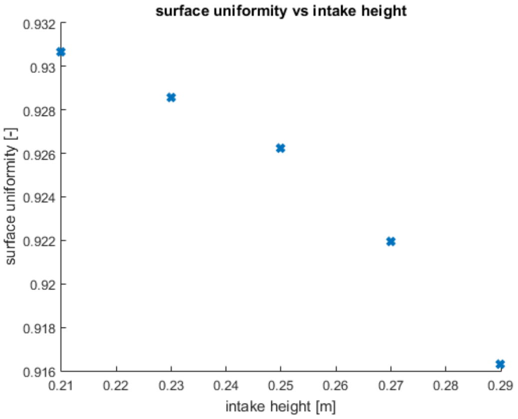

(a) Surface Uniformity vs intake height **(b)** Perpendicularity vs intake height

Figure 6.39: Surface Uniformity and Perpendicularity vs intake height

Figure 6.40 represents the thrust and torque comparison for each intake height. The lowest intake height has the lowest torque value and also has the highest thrust summation value. This is the reason why the efficiency of the lowest intake height of 0.21 m differs a lot from the largest intake height of 0.29 m.

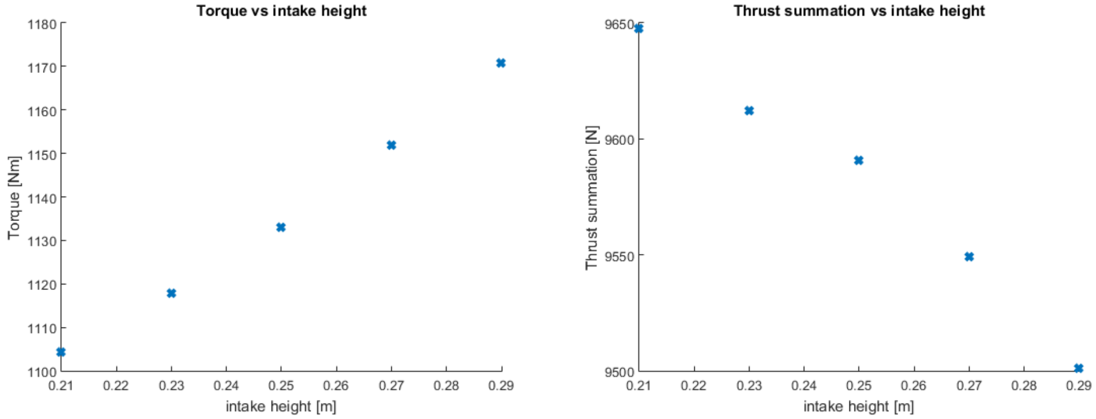

(a) Torque vs intake height **(b)** Thrust Summation vs intake height

Figure 6.40: Thrust and Torque vs intake height

The inflow to the pump is more uniform when the intake height is lower. This is frankly shown in fig. 6.41. The axial velocity field at the bottom of the section is very high for the height of 0.29 m compared to the height of 0.21 m. In addition, the axial velocity field at the top of the section is drastically low for the height of 0.29 m compared to the height of 0.21 m. It can be said that the inflow to the pump at a height of 0.21 m is more uniform compared to the heights of 0.25 m and 0.29 m.

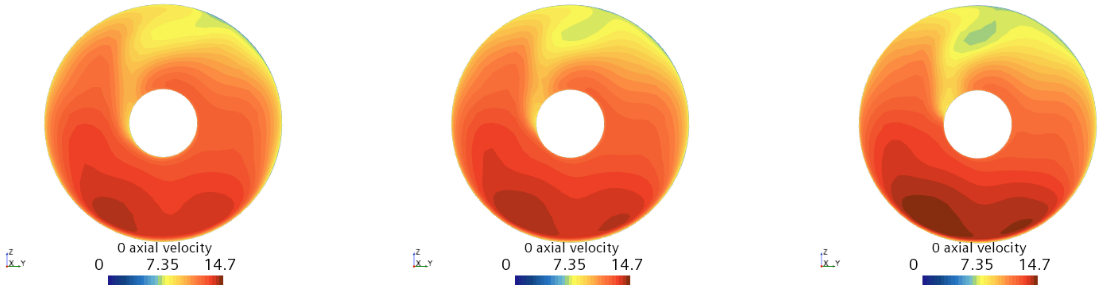

(a) height = 0.21 m **(b)** height = 0.25 m **(c)** height = 0.29 m

Figure 6.41: axial velocity vs intake height

Figure 6.42 presents the ratio of the tangential velocity to the axial velocity (V_t/V_a). The higher intake height the tangential velocity component and V_t/V_a are higher and will affect the inflow to the pump. The tangential velocity can happen due to the shaft rotation and the vertical momentum that the flow needs to move upward following the intake shape. In addition, when the axial velocity component is lower, it is easier to get disturbed by the shaft rotation effect.

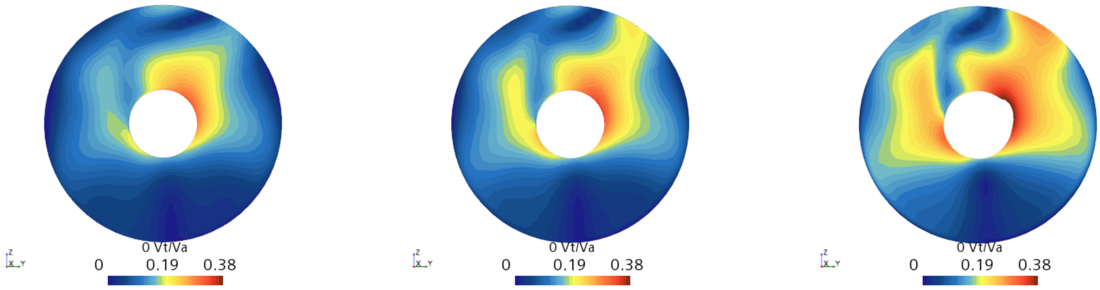

(a) height = 0.21 m **(b)** height = 0.25 m **(c)** height = 0.29 m

Figure 6.42: V_t/V_a vs intake height

6.12.2 Cross section

After carrying out the cross section optimization with three input parameters, the sensitivity analysis can be extracted for each parameter. The first parameter is the start tangential angle for the weight top. Figure 6.43 shows that the lower this angle the efficiency, which is thrust-over-torque parameter, tends to be better. It supports the idea that the hydrodynamic performance should be better when the fluid is moving on a more smooth surface (less sharp corner). The efficiency in fig. 6.43 shows a negative sign because of the optimization scheme from CAESES, so the sign can be negligible. In addition, many designs are performed around the start tangential angle of 22 deg because of the optimization algorithm nature that tries to refine the parameter quantity there to achieve the best design. The trend lines are obtained from CAESES as they show the parameter regression lines in both linear and high-order curves.

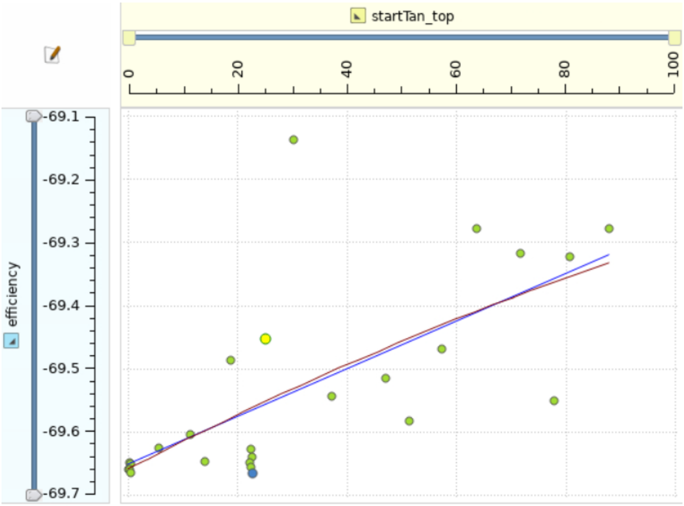

Figure 6.43: Sensitivity analysis of start tangential angle top

Next, the sensitivity analysis for the weight top factor is plotted in fig. 6.44. The higher the weight top factor, the less circular cross sections are generated. This results in the worse hydrodynamic performance of the flow. This plot shows that the lower the weight top factor, the better efficiency is gained.

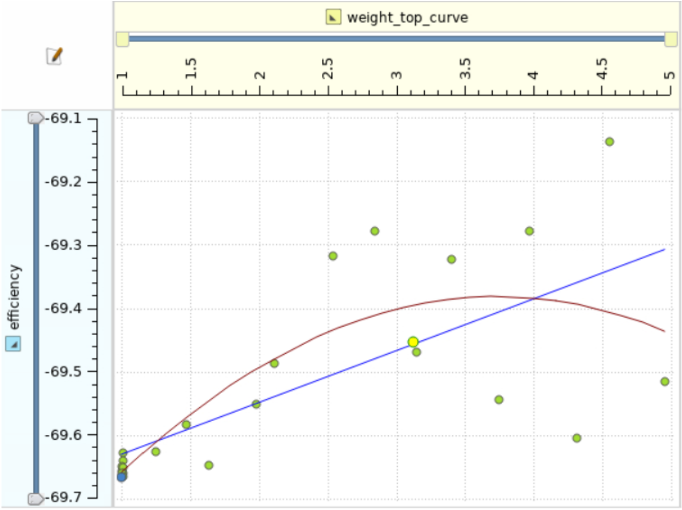

Figure 6.44: Sensitivity analysis of weight top factor

Finally, the sensitivity analysis for the weight top area adjust factor is plotted in fig. 6.45. If this factor is lower, the transition of the circular cross section will slow down and result in better flow behavior.

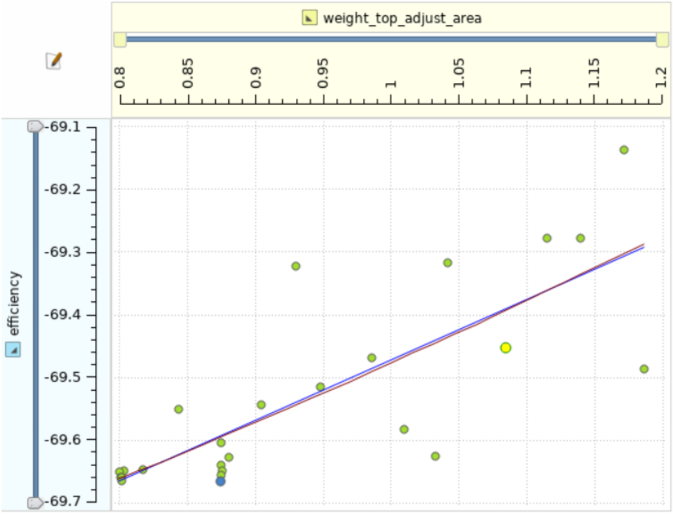

Figure 6.45: Sensitivity analysis of area adjust factor

15 samples are generated randomly to initialize the optimization study. After that, the optimization algorithm will run 10 iterations, moving toward the best design as shown in fig. 6.46. Thus, 25 simulations are performed in total. The best design is found in design number 18. Since this is not multi-objective optimization, no Pareto frontier is needed. No trend is shown here because all designs are randomly generated for each simulation.

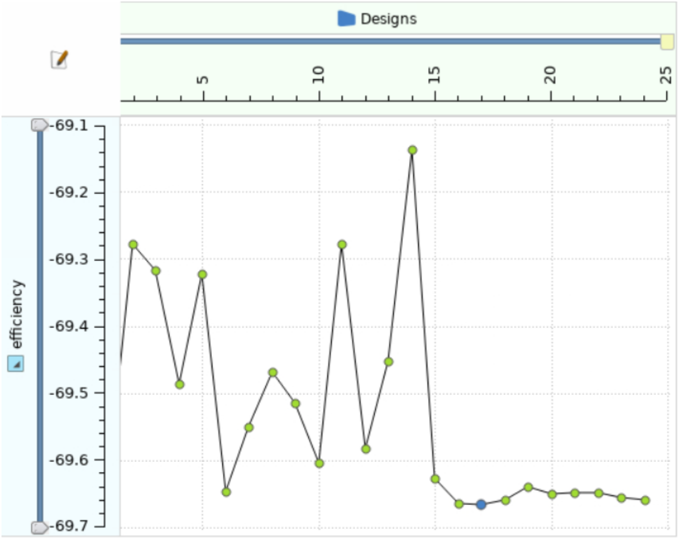

Figure 6.46: Intake cross section Optimization

After the optimization is done, the best intake design is compared to the original intake as shown in table 6.7. The system efficiency has improved by 4%. The trust summation is higher, while torque is lower. It can be seen that the best intake design gives the best inflow to the pump, including surface uniformity and perpendicularity.

parameters	Values		units
	Original intake	Optimized intake	
System efficiency	72.4	76.4	%
Thrust-over-Torque	66.2	69.7	%
Thrust summation	9578	9659	N
Torque	1148.2	1100.8	Nm
surface uniformity	0.923	0.928	-
perpendicularity	82.3	83.4	deg

Table 6.7: Results comparison between original and optimized intake design

Table 6.8 depicts the values of the studied parameters between the best intake design and the original intake design. The intake shape can be observed more in detail in fig. 6.47, 6.48, 6.49, and 6.50. To sum up, the best intake design has a lower height than the original one and also has a cross section that is more circular. From the optimization study, the intake height has the most dominant effect on the efficiency, while the cross section has less effect on the system efficiency, which is varied only in the range of 1%.

parameters	Values		units
	original intake	optimized intake	
intake height	0.265	0.21	m
start tangential angle for the weight top	45	22.7	deg
weight top factor	3	1	-
weight top area adjust factor	1	0.875	-

Table 6.8: Optimized intake and original intake parameters comparison

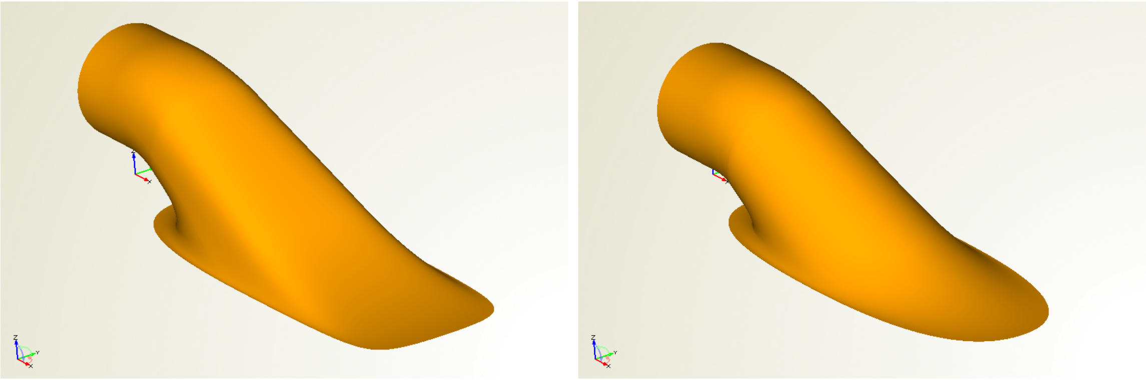

(a) Original intake **(b)** Optimized intake

Figure 6.47: Intake shape comparison (Perspective view)

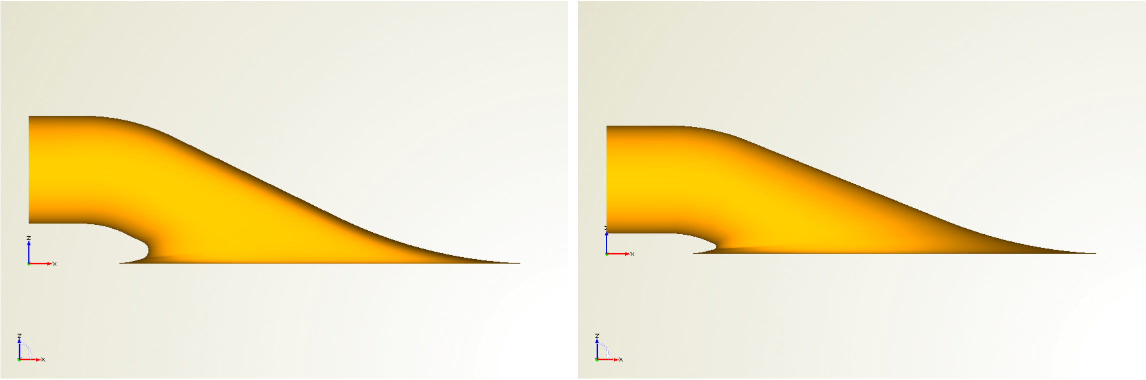

(a) Original intake **(b)** Optimized intake

Figure 6.48: Intake shape comparison (Side view)

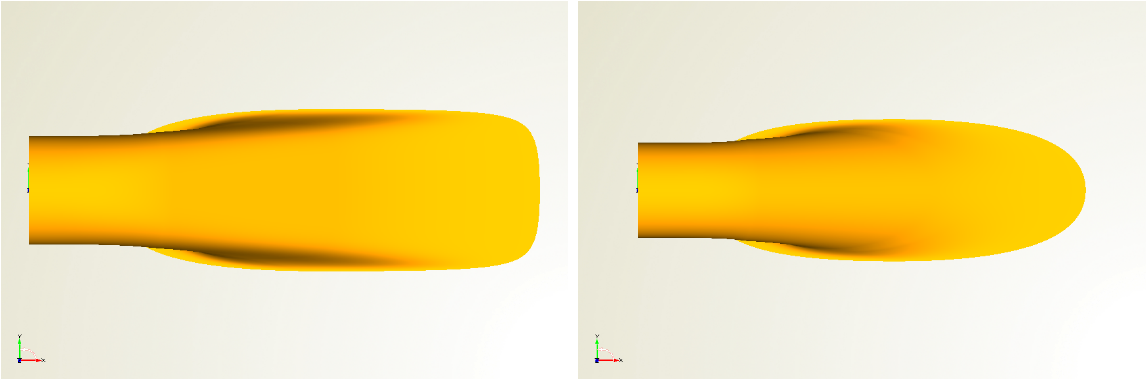

(a) Original intake **(b)** Optimized intake

Figure 6.49: Intake shape comparison (Top view)

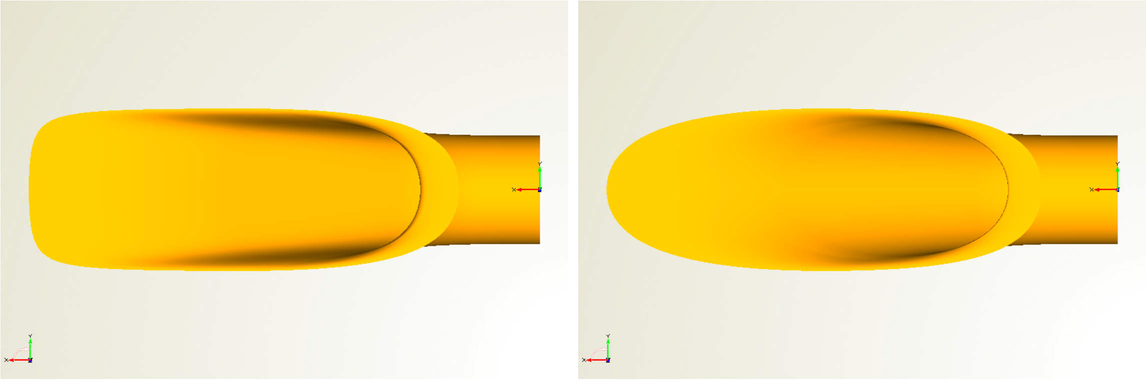

(a) Original intake **(b)** Optimized intake

Figure 6.50: Intake shape comparison (Bottom view)

The wake field for the optimized intake is more uniform as shown in fig. 6.51. The axial velocity field at the bottom of the section for the original intake is higher than the optimized intake. Furthermore, the axial velocity field at the top of the section for the original intake is lower than the optimized intake, as the light blue color can be observed from the contour plot. The shaft rotation effect is lower in the optimized intake as V_t/V_a field has lower component values compared to the original one, as shown in fig. 6.52. In addition, the tangential velocity component of the original intake is higher than the optimized intake because the flow is moving upward due to the larger height. This results in the higher velocity in the z axis.

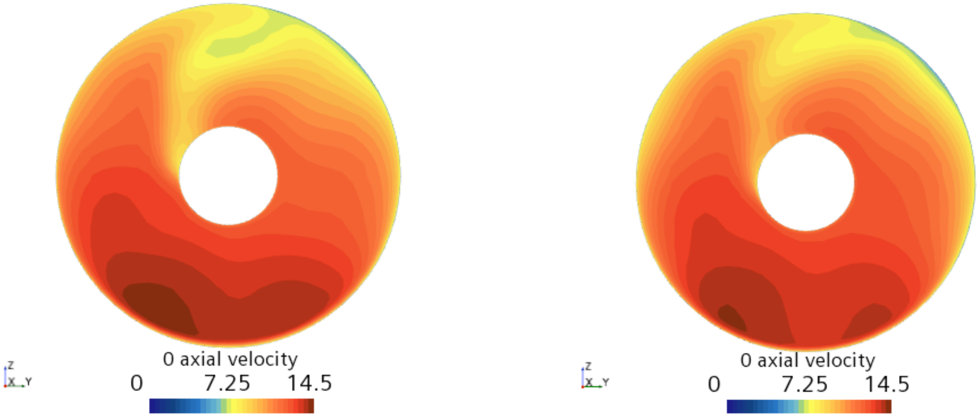

(a) Original intake **(b)** Optimized intake

Figure 6.51: Axial velocity at the pump upstream cross section comparison

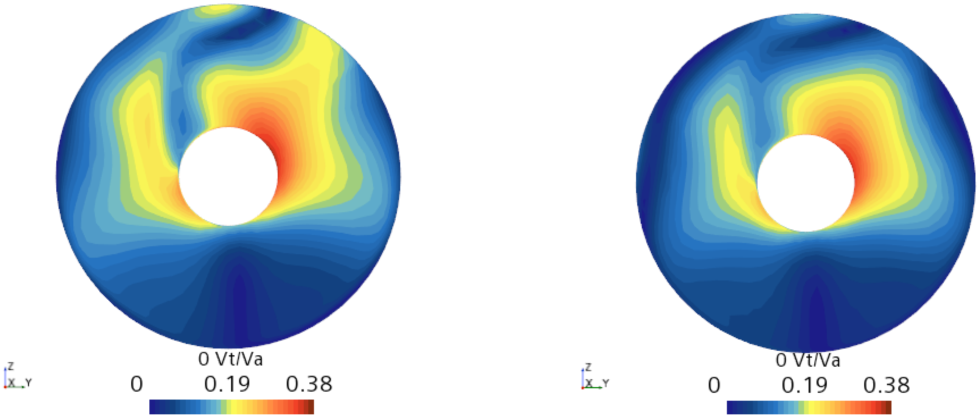

(a) Original intake **(b)** Optimized intake

Figure 6.52: V_t/V_a at the pump upstream cross section comparison

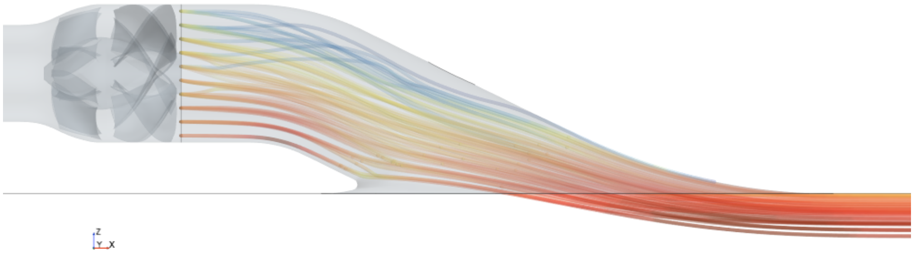

Figure 6.53: Streamline for the original intake to the rotor

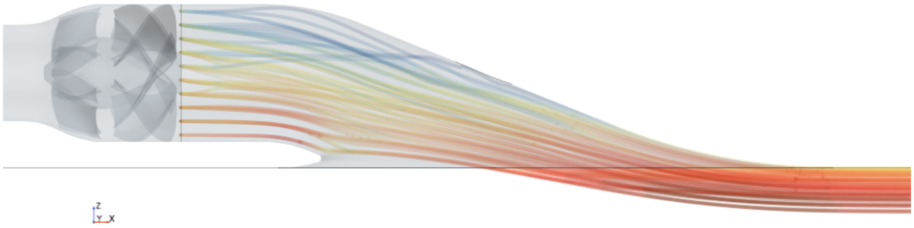

Figure 6.54: Streamline for the optimized intake to the rotor

6.12.3 Shaft Removal study for the best design

The shaft line from the best intake design has been removed and studied. The performance comparison between shaft-existing and shaft removal conditions is shown in table 6.9. The system efficiency and thrust-over-torque remain almost constant. However, the thrust summation for the shaft removal condition is higher by about 3.6%. Torque is also higher for the shaft removal condition, by roughly 3%. Because both the nominator and the denominator are changing in the same way, the efficiency does not change much.

parameters	Values		units
	shaft existing	without shaft	
System efficiency	76.4	76.5	%
Thrust-over-Torque	69.7	70.1	%
Thrust summation	9659	10002	N
Torque	1100.8	1132.7	Nm

Table 6.9: Results for the optimized intake comparison between shaft-existing and shaft removal conditions

Figure 6.55 shows the axial velocity field at the pump upstream cross section comparison between shaft-existing and shaft removal conditions. It can be seen that no shaft rotation effect is observed in the shaft removal condition. The wake fields between both conditions are totally different. This results in a different angle of attack for the blades. The axial velocity component for the shaft removal condition is gradually lower than for the shaft-existing condition. Thus, the angle of attack is higher in the shaft removal condition and results in higher thrust and torque. The trend is still similar as studied before in section 6.8.

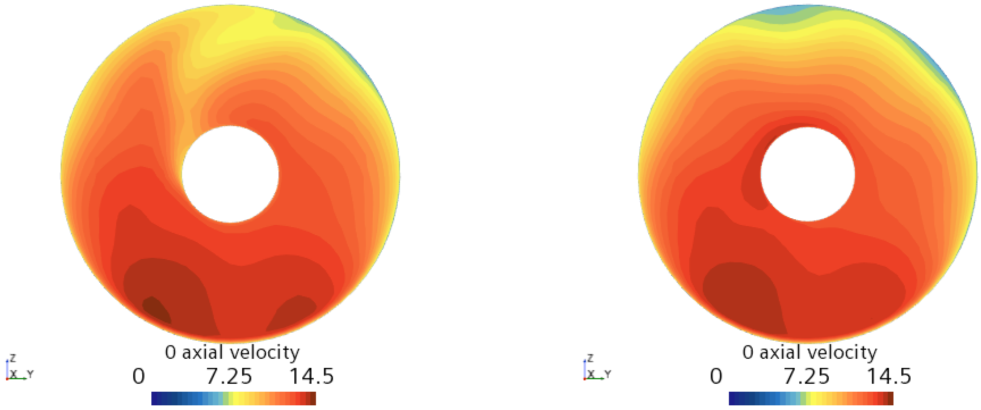

(a) Optimized intake with shaft **(b)** Optimized intake without shaft

Figure 6.55: Axial velocity at the pump upstream cross section comparison between shaft-existing and shaft removal conditions

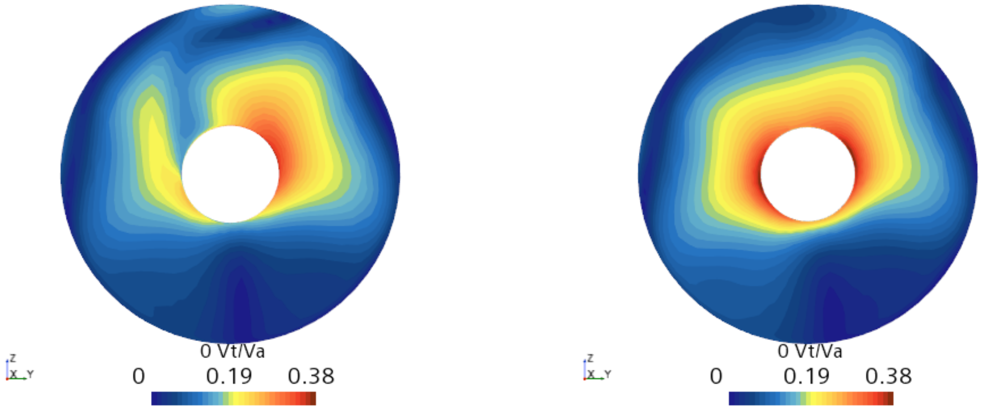

(a) Optimized intake with shaft **(b)** Optimized intake without shaft

Figure 6.56: V_t/V_a at the pump upstream cross section comparison between shaft-existing and shaft removal conditions

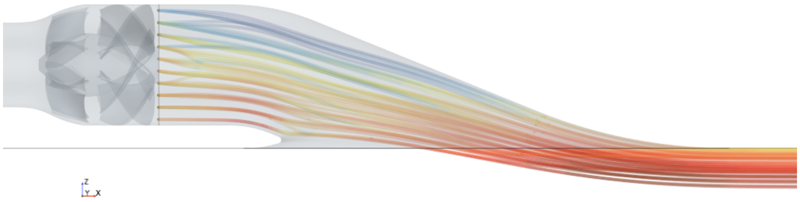

Figure 6.57: Streamline for the optimized intake without shaft to the rotor

7

Discussion

This section provides a discussion regarding the results presented in the previous chapter. System performance curve, extending pump-intake connection, shaft removal, rim-driven impeller, and intake optimization are discussed in more detail.

7.0.1 System Performance Curve

It is found that the mass flow rate of 761.9 kg/s is the best operating point for the system. The inlet velocity ratio (V_{pump}/V_{ship}) for this mass flow rate is equal to 0.7. Huang et al. (2019) recommends that the inlet velocity ratio of 0.6 to 0.8 is the suitable operating condition, otherwise, the hydraulic efficiency will drop drastically. In addition, the jet velocity ratio (V_{in}/V_{out}) for this mass flow rate is equal to 0.7, where V_{in} is measured at the capture area and V_{out} is measured at the nozzle exit. Bulten (2006a) recommends that the typical values of this ratio are in the range of 0.5 to 0.7. Therefore, the results from the system performance curve are quite reliable.

From the results, it is found that a low inlet velocity ratio will have poor uniformity and the flow separation will occur at the top of the ramp region. A high inlet velocity ratio will have better uniformity. However, it should be noted that this study assumes the flow to be non-cavitating. Normally, if the inlet velocity ratio is too high cavitation may occur.

7.0.2 Extending Pump-Intake Connection

First of all, it has to be noted that the AxWJ-2 pump is designed to work in a horizontal straight pipe condition. The performance of this pump can reach approximately 90%. This is proven by the simulation for a setup without intake. Therefore, it is clearly seen that the intake is the main reason for degrading the entire system's performance. In order to improve efficiency, the pump-intake connection was introduced. As shown by the higher pump inflow uniformity and perpendicularity values, the inflow to the pump is improved by extending the pump-intake connection. The flow non-uniformities are mixed out in the horizontal circular part of the duct. A longer pump-intake connection results in a more uniform flow as well as a more perpendicular flow into the pump.

Because of the S-formed intake shape, it results in a higher velocity field at the bottom, while the lower velocity field can be observed at the top. The wake field is obviously different between intake and without intake simulations. It can be said that the intake is a remarkably important factor in how the wake field for the system will be, so the pump model and the intake shape have to be designed together.

7.0.3 Shaft Removal

Although the efficiency for both cases is quite similar, the results show that the thrust summation for the shaft removal condition is quite higher than the shaft-existing condition. The wake fields between the shaft-existing and shaft removal conditions are totally different and lead to the different thrust and torque values. It can be said that the waterjet propulsion for the shaft removal condition can produce more thrust than the shaft-existing condition, but more power is required to reach the same ship speed. Based on this case study, the ship with a shaft removal waterjet propulsion system could be useful for the heavier ship.

From this study, it is evident that a different wake field to the pump can cause different pump performance. The wake field can be affected by the intake shape and the shaft. Thus, the impeller and stator blades have to be designed to work in a certain wake field. Two different pumps will not perform in a similar way in the same intake, and two intake shapes will cause different performances for the same pump.

7.0.4 Rim-driven Impeller

Normally, lower tip clearance results in better performance of the pump. The tip leakage phenomenon is reduced significantly by minimizing the tip gap (Martinsson and Varosy, 2017). However, the results show that the efficiency is worse when the tip gap is closed. This happens because of the rim-driven function that the pump housing is rotated. It causes the higher torque value needed to rotate this housing. The wake fields between having a tip gap and having no tip gap are similar because the intake shapes are the same and in both cases, the motor does not have a shaft. Thus, it is clearly seen that the rotating pump housing affects the performance. To overcome this issue, the blades have to be redesigned in order to operate suitably with the rim-driven behavior, as it can be seen from the market that many blade designs for the rim-driven pump are special and some of them do not have the hub.

7.0.5 Intake optimization

Regarding the intake height optimization, it is noticed that the tangential velocity component significantly degrades the system efficiency. This tangential velocity component is generated by the shaft rotation and the intake shape. When the height is reduced, the flow velocity in the z-axis decreases. This is the main reason for the better performance with the lowest intake height. As mentioned before, this pump is designed to work in a horizontal straight pipe condition. Thus, lowering the intake height will make the flow behavior more similar to the fluid flowing through the horizontal pipe. It can be seen that the wake field is different between each intake height and this results in different efficiency.

According to the cross-section optimization, the efficiency changes gradually during the optimization. The cross section is insensitive to the system's efficiency. However, the result shows that the intake shape with less sharp corner cross sections gives the best hydraulic performance. Finally, thrust-over-torque can be used to run the optimization for studying the intake geometry as it can represent the way system efficiency changes without performing capture area extraction.

8

Conclusion

It is concluded that increasing the pump-intake connection length and lowering the intake height improves the overall performance of the system. This behavior can be related to the horizontal straight pipe setup. The flow becomes more similar to the optimal pump design condition of a horizontal setup as the intake is lowered and the intake connection is lengthened. Two factors can be used as indicators of this optimal condition: flow perpendicularity and uniformity.

The wake fields from the shaft-existing and shaft removal conditions are totally different because of the shaft rotation effect. This results in different pump performances and confirms the previous conclusion on the interaction between the wake field and the pump design. Similar to that, the rim-driven option is one of the future options for electric waterjets. This solution provides opportunities to reduce the intake height. However, the blades need to be redesigned to adapt to the actual flow into the pump to achieve the best performance.

There is a clear interaction effect between the intake and the pump design, so close collaboration between these two design loops improves system performance. Unfortunately, AxWJ-2 pump is the only pump that this project uses to optimize the intake geometry. Moreover, time is one of the big limitations, so no new impeller design is performed to suit the wake field generated by the final obtained intake.

9

Future Work

After finalizing the research, further investigation should be done to answer the last remaining questions of the master's thesis. As concluded previously, it is believed that the performance of the waterjet system is not optimal due to the chosen impeller, which is designed for a horizontal straight pipe condition. To verify this hypothesis, future work will comprise the design of a pump impeller for a given wake, starting from a specific intake design.

This future work would prove or clarify whether the impeller design highly affects the pump performance or not. For instance, a starting point could be by making an impeller blade design for the final optimized intake presented in this report and measuring how the system efficiency changes. It is believed that further investigation could bring interesting discussions on how to approach waterjet design in the future.

In addition, for two waterjets, merging two intakes is an interesting thing to do in the future. This can reduce the wetted surface. It means that the system will have a less frictional loss. The water mass might be reduced inside the intake and result in a lighter weight for a vessel. Another step that the next project could consider is changing the intake shape to be like a diffuser. The diffuser intake will draw the water to the pump at a lower velocity than usual. This may result in increased boundary layer ingestion (flow with lower momentum flux) which in turn can result in higher thrust with the same shaft-delivered power.

Bibliography

N. Budziszewski and J. Friedrichs. Modelling of A Boundary Layer Ingesting Propulsor. *Energies*, 11(4)(708), 3 2018.

N. Bulten. *Numerical analysis of a waterjet propulsion system.* PhD thesis, Technische Universiteit Eindhoven., Eindhoven., 2006a.

N. W. H. Bulten. Waterjet propulsion theory. In *Numerical Analysis of a Waterjet Propulsion System*, chapter 2. Printservice Technische Universiteit Eindhoven, Eindhoven, The Netherlands, 2006b.

CAESES. CAESES , 2019.

J. Carlton. Waterjet Propulsion. In *Marine Propellers and Propulsion*, chapter 16. Oxford, UK, 2012.

Eca L. and M. Hoekstra. A procedure for the estimation of the numerical uncertainty of CFD calculations based on grid refinement studies. *Journal of Computational Physics*, 262, 4 2014.

A. Eslamdoost. *The Hydrodynamics of Waterjet/Hull Interaction* . PhD thesis, Chalmers University of Technology, Gothenburg, Sweden, 2014.

A. Eslamdoost and M. Vikström. Body-force model for waterjet pump simulation. *Applied Ocean Research*, 90, 2019.

R. Huang, Y. Dai, X. Luo, Y. Wang, and C. Huang. Multi-objective optimization of the flush-type intake duct for a waterjet propulsion system. *Ocean Engineering*, 187:106172, 9 2019. ISSN 0029-8018. doi: 10.1016/J.OCEANENG.2019.106172.

D. Jiang-ming and W. Yong-sheng. *Research on Flow Loss of Inlet Duct of Marine Waterjets.* PhD thesis, Shanghai Jiaotong University and Springer-Verlag Berlin Heidelberg, Wuhan, China, 2010.

E. Krause. Fluid mechanics: with problems and solutions, and an aerodynamic laboratory. 2005.

C. Liu, Y. Wang, Z. Zhang, and J. Liu. Research on effect of different flow control volume on waterjet perforance prediction. *J. Ship Mechanics*, 14 (10)(1117-1121), 2010.

H. Martinsson and J. Varosy. *CFD simulation of the Wakejet flow.* PhD thesis, CHALMERS UNIVERSITY OF TECHNOLOGY, Gothenburg, 2017.

K. Moon-Chan and Chun Ho-Hwan. Experimental Investigation into the performance of the Axial-Flow-Type Waterjet according to the Variation of Impeller Tip Clearance. Technical report, Department of Naval Architecture and Ocean engineering., Pusan, Korea, 2005.

Siemens. STARCCM+ . 2018.

T. Takai. *Simulation based design for high speed sea lift with waterjets by high fidelity urans approach.* PhD thesis, University of Iowa, Iowa, 2010.

M. Thad J, S. Seth D, and B. Alan J. Design of the ONR AxWJ-2 Axial Flow Water Jet Pump. Technical report, Naval Surface Warfare Center, West Bethesda, MD, 11 2008.

Weixuan Jiao, Li Cheng, Di Zhang, Bowen Zhang, Yeping Su, and Chuan Wang. Optimal Design of Inlet Passage for Waterjet Propulsion System Based on Flow and Geometric Parameters. *Advances in Materials Science and Engineering*, 2019 (2320981), 5 2019.

F. M. White. *Fluid Mechanics.* USA, 7th edition, 2011.

A

Appendix 1

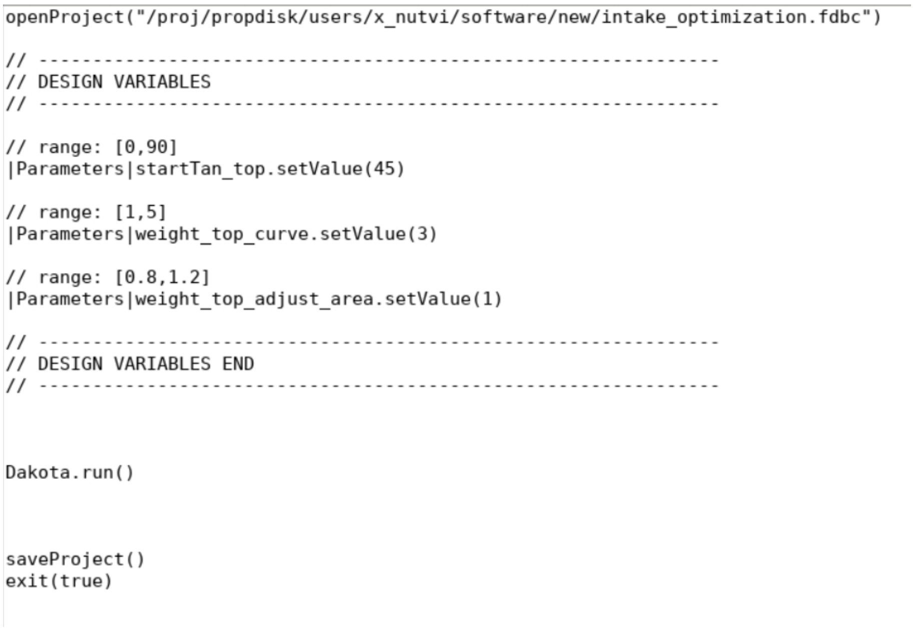

```
openProject("/proj/propdisk/users/x_nutvi/software/new/intake_optimization.fdbc")

// ---------------------------------------------------------------
// DESIGN VARIABLES
// ---------------------------------------------------------------

// range: [0,90]
|Parameters|startTan_top.setValue(45)

// range: [1,5]
|Parameters|weight_top_curve.setValue(3)

// range: [0.8,1.2]
|Parameters|weight_top_adjust_area.setValue(1)

// ---------------------------------------------------------------
// DESIGN VARIABLES END
// ---------------------------------------------------------------



Dakota.run()



saveProject()
exit(true)
```

Figure A.1: Cross section optimization execution script

DEPARTMENT OF MECHANICS & MARITIME SCIENCES
CHALMERS UNIVERSITY OF TECHNOLOGY
Gothenburg, Sweden
www.chalmers.se

CHALMERS
UNIVERSITY OF TECHNOLOGY